Available online at www.sciencedirect.com

ScienceDirect

Journal of Catalysis 256 (2008) 108–125

JOURNAL OF CATALYSIS

www.elsevier.com/locate/jcat

New insights into the nature of the acidic catalytic active sites present in ZrO_2-supported tungsten oxide catalysts

Elizabeth I. Ross-Medgaarden [a], William V. Knowles [b], Taejin Kim [a], Michael S. Wong [b,c], Wu Zhou [d], Christopher J. Kiely [d], Israel E. Wachs [a,*]

[a] *Operando Molecular Spectroscopy & Catalysis Laboratory, Department of Chemical Engineering, Lehigh University, Bethlehem, PA 18015, USA*

[b] *Department of Chemical and Biomolecular Engineering, Rice University, Houston, TX 77005, USA*

[c] *Department of Chemistry, Rice University, Houston, TX 77005, USA*

[d] *Center for Advanced Materials and Nanotechnology, Department of Materials Science & Engineering, Lehigh University, Bethlehem, PA 18015, USA*

Received 10 January 2008; revised 4 March 2008; accepted 5 March 2008

Available online 10 April 2008

Abstract

An extensive series of supported $WO_3/ZrO_x(OH)_{4-2x}$ catalysts (WZrOH) were synthesized by standard aqueous impregnation of ammonium metatungstate into an amorphous $ZrO_x(OH)_{4-2x}$ metastable support, followed by high-temperature calcination (at 773–1173 K). The supported WZrOH catalysts were also compared with well-defined model supported WO_3/ZrO_2 catalysts ($WZrO_2$) consisting of a thermally stable crystalline m-ZrO_2 support. Both series of supported tungsten oxide catalysts were physically characterized (by XRD, XPS, TEM, *in situ* Raman, and *in situ* UV–vis spectroscopy) and chemically probed by methanol dehydration (i.e., TPSR spectroscopy and steady-state catalytic studies). Monolayer surface WO_x coverage was found to occur at ~4.5–5 W-atoms/nm^2 for both catalytic systems. Whereas the dehydrated model supported $WZrO_2$ series contained only surface WO_x species below monolayer coverage, the dehydrated supported WZrOH series had the same surface WO_x species, as well as some Zr-stabilized distorted WO_3 nanoparticles (NPs). Above monolayer coverage, the model supported $WZrO_2$ catalysts contained only ordered crystalline WO_3 NPs, but the supported WZrOH catalysts had both ordered WO_3 NPs and Zr-stabilized distorted WO_3 NPs. The comparative methanol dehydration to dimethyl ether acidity study revealed that the Zr-stabilized distorted WO_3 NPs were the catalytic active sites in supported WZrOH catalysts. These findings represent a new model for the origin of the enhanced solid acidity of supported WZrOH catalysts.

Keywords: Catalysts, supported, oxides, WO_3, ZrO_2; Reaction, CH_3OH, dehydration, CH_3OCH_3, DME; Spectroscopy, *in situ*, Raman, UV–vis, XPS; Electron microscopy, TEM, HREM imaging

1. Introduction

Zirconia-supported tungsten oxide catalysts have received much attention in the recent catalysis literature due to their industrial application for converting C_4–C_8 paraffins to highly branched species that upgrade the gasoline octane number [1–11]. Supported WO_x/ZrO_2 catalysts also show commercial promise for such major industrial applications as selective catalytic reduction of NO_x to N_2 [12,13], xylene formation from toluene and methanol [14], oligomerization of $<C_{20}$ alkanes to gasoline, diesel and lubricants (C_{30+}) [15], and the removal of sulfur- and nitrogen-containing impurities ("hydrotreating") from hydrocarbon streams when combined with a hydrogenation/dehydrogenation component, such as Pt [16]. For many of these catalytic applications, the solid acidity of the supported tungsten oxide phase plays a crucial role in the overall catalytic performance.

There seems to be a general agreement in the literature that the maximum reactant turnover rates occur at "intermediate" surface tungsten densities (W-atoms/nm^2): ~6–8 W/nm^2 for *n*-pentane isomerization [2,17], and ~7–8 W/nm^2 for *o*-xylene isomerization [18–20], as well as 2-butanol dehydration [21]. "Intermediate" is loosely defined as the W/nm^2 range that

* Corresponding author. Fax: +1 (610) 758 6555.
E-mail address: iew0@lehigh.edu (I.E. Wachs).

0021-9517/$ – see front matter © 2008 Elsevier Inc. All rights reserved.
doi:10.1016/j.jcat.2008.03.003

maximizes the population of amorphous surface polytungstate species relative to isolated surface WO_x and WO_3 nanocrystalline domains. Absolute values for the minimum and maximum surface densities that bracket this range differ between reactions and even differ within a given reaction, depending on operating conditions and the basis of measurement. Most researchers agree that regardless of the exact numerical W/nm^2 value, the effective upper end of the "intermediate" range corresponds to the formation of WO_3 nanocrystallites.

Multiple catalytic active sites have been proposed for supported WO_x/ZrO_2 catalysts [2,17–19,22,23], but supporting information for the nature of the true catalytic active phase is lacking. Most previous studies used a wide variety of characterization techniques and catalytic testing to describe the composition, oxidation state, coordination and nature of acidity (Brønsted vs Lewis) of the tungsten oxide species participating as the catalytic active sites. The following catalytic active site models have been proposed: (i) fully oxidized, noncrystalline surface polytungstate networks incorporating trace levels of surface-exposed Zr capable of stabilizing delocalized protons (Brønsted acidity) similar to that of heteropolyacids [17,25]; (ii) highly polymerized oxyanions of slightly reduced tungsten oxide formed *in situ* to stabilize delocalized protons (Brønsted acidity) on $H^{\delta+}(O_3)_n^{\delta-}$ domains [18–21,23,24,26,27]; and (iii) catalysts with intermediate tungsten oxide loadings that generate nearly a 1:1 ratio of strong Brønsted acid sites to Lewis acid sites, although the origin of the surface acid sites (W or Zr cations) is not known [2,28,29].

Based on the trend of reactivity versus tungsten oxide structure, the growing literature consensus is that the catalytic active site(s) responsible for high surface acidic activity form with a maximum in surface polytungstate (WO_x) concentration. The maximum amount of surface polytungstate species should occur at monolayer surface tungsten oxide coverage, but very different models for surface polytungstate monolayer coverage have been proposed. The support layer geometry monolayer (ML) models assume epitaxial-like growth of the surface tungsten oxide overlayer without considering possible chemical interactions (e.g., coordination, steric hindrance, repulsion) at the surface layer. Based on the (001) projection of ZrO_2 [30], a tungstate ML was calculated as ~7.3 W-atoms/nm^2 [2,31], in which the WO_6 octahedra are presumably anchored to exposed Zr–OH sites [32]. Other models concentrate on the surface layer geometry and are support-independent, disregarding how the surface tungsten oxide species and the underlying support oxide are bound together [22,33–35]. One such model envisions surface saturation of the supported metal oxide layer as a two-dimensional close packing of monomeric sites [22,33–35]. For bulk WO_3, a close packing was calculated as 0.21 g $WO_3/(100\ m^2)$, which is equivalent to ~5.5 W-atoms/nm^2 [33–36]. Another model estimates surface saturation of the WO_3 at ~6.4 W-atoms/nm^2 based on the bulk density of WO_3 [25], and yet another model estimates the ML at ~7.8 W-atoms/nm^2 by estimating the density of WO_x species in a two-dimensional plane of corner-shared WO_6 octahedra [2].

In contrast to the foregoing "theoretical" ML models that assume a specific structure for a surface tungsten oxide species, experimental XPS, ISS, and Raman spectroscopic measurements have demonstrated that ML coverage actually corresponds to 4–5 W-atoms/nm^2 [36–38] for surface WO_x on all oxide supports, with the exception of the weakly interacting supported WO_3/SiO_2 catalyst system, where tungsten oxide dispersion is very poor. The foregoing literature review of supported WO_x/ZrO_2 catalysts reveals a lack of agreement concerning several critical issues regarding the tungstated zirconia system. Despite several papers devoted to the physical and chemical characterization of supported WO_3/ZrO_2 catalysts, the issues of surface tungsten oxide ML coverage and the nature of the catalytic active acidic sites remain unresolved.

The present investigation was undertaken to investigate the structure–property relationship of supported WO_x/ZrO_2 catalytic materials and their acidic characteristics for methanol dehydration. The study used zirconium oxyhydroxide supported tungsten oxide to (i) identify the surface WO_x molecular structures present on ZrO_2 as a function of surface W/nm^2 density, (ii) determine the surface W/nm^2 density corresponding to surface WO_x monolayer coverage on ZrO_2, (iii) investigate the surface acid catalysis of supported WO_x/ZrO_2 with the methanol chemical probe molecule, and (iv) identify the nature of the catalytic active site(s) present for supported WO_x/ZrO_2 catalysts. The findings with zirconium oxyhydroxide-supported tungsten oxides (WZrOH) are also critically compared with the previously published findings for the model supported WO_3/ZrO_2 system ($WZrO_2$), in which the starting ZrO_2 support is already present as a crystalline material [37,38].

2. Experimental

2.1. Catalyst synthesis

2.1.1. Preparation of the $ZrO_x(OH)_{4-2x}$ support

Zirconium oxyhydroxide was prepared by a method similar to that described by Hino and Arata [1]. A completely dissolved solution of 313.3 g $ZrOCl_2{\cdot}8H_2O$ (Aldrich, 98%) in 0.7 L of deionized water (room temperature, final solution pH ~1) was added dropwise over ~1 h into 600 mL of deionized water, with 15.8 M of NH_4OH added as necessary to maintain batch $10 \leqslant pH \leqslant 11$, resulting in immediate precipitation of a buoyant white powder. After stirring for 24 h at room temperature, the precipitate was dried in static air at 343 K, crushed, sieved (to <170 mesh), and redispersed in 1.8 L of deionized water at pH ~10 for 30 min before separation. Multiple redispersions and filtrations were performed until the supernatant chloride ion concentration reached that of the water background, as verified by $AgNO_3$ titration with K_2CrO_4 indicator. Finally, the powder was dried overnight in static air at 343 K before being crushed and sieved (to <170 mesh).

2.1.2. Preparation of supported $WO_3/ZrO_x(OH)_{4-2x}$

The $ZrO_x(OH)_{4-2x}$ support was hand-mixed for ~1 h after sieving to <170 mesh to homogenize the master batch. Before incipient wetness impregnation, the support was dried overnight in static air at 343 K to remove adventitious moisture. Tungstated-zirconia catalysts with various weight percentages (5.1, 10.1, 15, 19.5, 23.3, and 26.6%) were prepared by incipient-wetness impregnation of aqueous solutions of ammonium metatungstate $(NH_4)_{10}W_{12}O_{41}\cdot 5H_2O$ (Osram Sylvania, 98% purity). The zirconia hydroxide support was impregnated to 95% pore volume (V_p) as determined by triple nitrogen physisorption analyses at 77 K (V_p at $P/P_0 = 0.984$, Micromeritics ASAP2010) and mixed for ∼30 min by hand to ensure uniform solution dispersion, with an average of $V_p = 0.17\ \text{cm}^3/\text{g}$. The tungstated zirconia samples were dried overnight at 343 K in static air, crushed, and sieved (to <170 mesh), then calcined at the desired temperature (773, 873, 973, 1073, and 1173 K) in static air for 3 h. The following notation is used to express the supported tungsten oxide samples: yWZrOH-$T(\rho_{\mathrm{W,surf}})$, where y is the loading of W as WO_3 (wt%), T is the calcination temperature (K), $\rho_{\mathrm{W,surf}}$ is the tungsten surface density (W-atoms/nm²), and ZrOH represents the amorphous zirconium oxyhydroxide ($ZrO_x(OH)_{4-2x}$) support precursor used. For example, 10.1WZrOH-1073(6.2) designates a $WO_x/ZrO_x(OH)_{4-2x}$ sample with 10.1% W that was calcined to 1073 K with a resulting $\rho_{\mathrm{W,surf}}$ of 6.2 W-atoms/nm². Surface tungsten oxide coverage and loading for the supported WO_3 catalysts are specified in Table 1. The $\rho_{\mathrm{W,surf}}$ for the WZrOH catalysts is based on a more general definition of surface density that uses the combined material surface area (i.e. the surface area of the calcined sample), because the amorphous $ZrO_x(OH)_{4-2x}$ support is sensitive to calcination temperatures. Because significant structural rearrangement and consequent loss of surface area occurred for $WO_x/ZrO_x(OH)_{4-2x}$ materials, the resulting $\rho_{\mathrm{W,surf}}$ of WZrOH and $WZrO_2$ catalysts discussed, are determined by the following equation:

$$\rho_{\mathrm{W,surf}}\left[\frac{\text{M atoms}}{\text{nm}^2\ \text{support}}\right] = \left\{(1\ [\text{g catalyst}])\left(\frac{\frac{\text{wt\% MO}_x}{100}}{1}\left[\frac{\text{g MO}_x}{\text{g catalyst}}\right]\right) \times\left(\frac{1}{\mathrm{M_W}}\left[\frac{\text{mol MO}_x}{\text{g MO}_x}\right]\right)\left(\frac{\nu_{\text{stoich}}}{1}\left[\frac{\text{mol M}}{\text{mol MO}_x}\right]\right) \times\left(\frac{6.022\times10^{23}}{1}\left[\frac{\text{M atoms}}{\text{mol M}}\right]\right)\right\}\Big/\left\{(1\ [\text{g catalyst}]) \times\left(\text{S.A.}_{\text{catalyst sample after calcination}}\left[\frac{\text{m}^2\ \text{support}}{\text{g support}}\right]\right) \times\left(\frac{10^9}{1}\left[\frac{\text{nm}}{\text{m}}\right]\right)^2\right\}. \tag{1}$$

Table 1

BET surface area and tungsten oxide surface density (W-atoms/nm²) of supported tungsten oxide on the $ZrO_x(OH)_{4-2x}$ support

Catalyst	WO_3 (wt%)	$T_{\text{calcination}}$ (K)	BET S.A. (m²/g)	$\rho_{\mathrm{W,surf}}$ (W-atoms/nm²)
5.1WZrOH-773(1.7)	5.1	773	75.8	1.7
5.1WZrOH-873(2.6)	5.1	873	51.6	2.6
5.1WZrOH-973(3.5)	5.1	973	37.5	3.5
5.1WZrOH-1073(4.3)	5.1	1073	30.7	4.3
5.1WZrOH-1173(5.9)	5.1	1173	22.6	5.9
10.1WZrOH-773(2.9)	10.1	773	89.1	2.9
10.1WZrOH-873(3.9)	10.1	873	66.5	3.9
10.1WZrOH-973(5.2)	10.1	973	50.3	5.2
10.1WZrOH-1073(6.2)	10.1	1073	42.1	6.2
10.1WZrOH-1173(9.8)	10.1	1173	26.9	9.8
15WZrOH-773(4.1)	15.0	773	96.0	4.1
15WZrOH-873(4.9)	15.0	873	80.0	4.9
15WZrOH-973(6.2)	15.0	973	62.8	6.2
15WZrOH-1073(8.4)	15.0	1073	46.2	8.4
15WZrOH-1173(15.8)	15.0	1173	24.7	15.8
19.5WZrOH-773(4.1)	19.5	773	123	4.1
19.5WZrOH-873(5.5)	19.5	873	91.4	5.5
19.5WZrOH-973(6.7)	19.5	973	75.2	6.7
19.5WZrOH-1073(10.6)	19.5	1073	47.9	10.6
19.5WZrOH-1173(20.2)	19.5	1173	25.1	20.2
23.3WZrOH-773(5.4)	23.3	773	113	5.4
23.3WZrOH-873(7.1)	23.3	873	85.7	7.1
23.3WZrOH-973(9.5)	23.3	973	63.6	9.5
23.3WZrOH-1073(14.0)	23.3	1073	43.1	14.0
23.3WZrOH-1173(24.1)	23.3	1173	25.1	24.1
26.6WZrOH-773(7.1)	26.6	773	97.8	7.1
26.6WZrOH-873(9.0)	26.6	873	76.8	9.0
26.6WZrOH-973(12.0)	26.6	973	57.4	12.0
26.6WZrOH-1073(17.1)	26.6	1073	40.5	17.1
26.6WZrOH-1173(29.4)	26.6	1173	23.5	29.4

2.1.3. Preparation of model supported WO_3/ZrO_2 catalysts

The support used for the model supported WO_3/ZrO_2 catalysts was ZrO_2 (Degussa, BET = 60 m²/g), which is known to have a well-crystallized monoclinic structure. Tungsten oxide-supported zirconia catalysts with varying surface densities were prepared by incipient-wetness impregnation of aqueous solutions of ammonium metatungstate, $(NH_4)_{10}W_{12}O_{41}\cdot 5H_2O$ (Pfaltz & Bauer, 99.5% purity) on the ZrO_2 support. The samples were first dried overnight under ambient conditions and then calcined in flowing air (Airgas, Zero Grade) at 723 K for 4 h. The following notation is used to express the supported tungsten oxide samples: xWZrO$_2$-$T(\rho_{\mathrm{W,surf}})$, where x is the loading of W as WO_3 (wt%), T is the calcination temperature (K), $\rho_{\mathrm{W,surf}}$ is the tungsten surface density (W-atoms/nm²), and ZrO_2 represents the crystalline ZrO_2 support. For example, 9.4WZrO$_2$-723(4.5) designates a model WO_x/ZrO_2 sample with 9.4% W that was calcined to 723 K with a resulting $\rho_{\mathrm{W,surf}}$ of 4.5 W-atoms/nm². Surface tungsten oxide coverage and loading for the model supported WO_3 catalysts have been published previously [37,38]. Although it was previously shown [37,38] that the crystalline ZrO_2 support exhibits negligible surface area loss with the impregnation of surface WO_x, the surface densities for the model supported $WZrO_2$ catalysts in this work are based on the calcined sample's final surface area, to be consistent with the surface density values reported for the supported WZrOH catalytic system.

2.2. Catalyst characterization

2.2.1. Elemental analysis

The elemental composition of select representative samples was measured via inductively coupled plasma–mass spectroscopy (ICP-MS) at Lehigh Testing Laboratories, Inc. (New Castle, DE) for calculation of the final wt% WO_3 loading. Excellent agreement was found between nominal and actual wt% WO_3 loadings.

2.2.2. BET specific surface area

The BET surface areas of the samples were determined by a 5-point BET correlation ($P/P_0 = 0.06$, 0.08, 0.12, 0.16, and 0.20) [41] for N_2 adsorption isotherms (77 K) collected on a Micromeritics ASAP 2010 using Matheson ultra-high-purity (UHP) N_2. Sample pretreatment involved evacuation at 523 K until the degas rate was $<3 \times 10^{-3}$ mm Hg/min. The instrument accuracy is approximately $\pm 1.3\%$ (relative standard deviation, $n = 44$) of measured value, with the instrument calibration verified by a SiO_2/Al_2O_3 reference standard.

2.2.3. X-ray diffraction

Powder X-ray diffraction (XRD) patterns were obtained with a powder diffractometer (Rigaku D/Max-2100 PC) using unfiltered CuK_α radiation ($\lambda = 1.5406$ Å) at 40 kV and 40 mA. Diffraction patterns were collected in continuous scan mode using a 0.02° step size and a ∼2.5 s/step scan rate. Goniometer alignment was verified by daily analysis of a Rigaku-supplied polycrystalline silicon reference standard.

For the pseudobinary combination of t-ZrO_2 and m-ZrO_2, an empirical relationship was used to estimate the relative volume fractions (V_i) of the two crystalline species ($V_m + V_t = 1$) using the integrated areas (I) of the ($\bar{1}11$) and (111) reflections for m-ZrO_2 and the (101) reflection for t-ZrO_2 using the following equations [40,41]:

$$X_m = \frac{I_m(\bar{1}11) + I_m(111)}{I_m(\bar{1}11) + I_m(111) + I_t(101)} \tag{2}$$

and

$$V_m = \frac{1.311 X_m}{1 + 0.311 X_m}. \tag{3}$$

This calculation cannot account for amorphous zirconia fractions, because they are not detectable by XRD.

2.2.4. Photoelectron spectroscopy

X-ray photoelectron spectroscopy (XPS) was performed on the supported WO_x/ZrO_2 and $WO_x/ZrO_x(OH)_{4-2x}$ samples using a Phi Quantera spectrometer equipped with an aluminum anode (Al$K_\alpha = 1486.6$ eV) operated at 25 W (15 kV, 1.67 mA) with a 100-µm spot size and 3-kV ion gun accelerating voltage. The experiments were performed in a conventional ultra–high-vacuum (UHV) chamber with a base operating pressure of typically $\sim 7 \times 10^{-6}$ N/m^2. Ambient-exposed, air-oxidized samples were compressed between two pieces of indium foil to minimize contamination, after which one of the powdered cake halves was mounted under a stainless steel bracket containing a 1-mm hole onto the sample platen. Equipment was not available to thermally dehydrate samples *in situ* within the XPS, so dehydration was achieved by holding at room temperature under UHV conditions. A minimum of 3 spots for each sample were simultaneously analyzed to test sample heterogeneity; the results reported here are averages of these multiple spots. A gold standard (binding energy, 84.2 eV) was used to verify instrument calibration. An Ulvac-Phi MultiPak nonlinear least squares curve-fitting program was used for data analysis with integral background.

2.2.5. Raman spectroscopy

Raman spectroscopy was used to obtain the molecular structures of the supported tungsten oxide catalysts with a visible (532 nm) laser excitation on a single-stage Horiba–Jobin Yvon Lab Ram-HR Raman spectrometer equipped with a confocal microscope (Olympus BX-30) and a notch filter (Kaiser Super Notch). The visible excitation was generated by a Nd-YAG doubled diode pumped laser (Coherent Compass 315M-150; output power, 150 mW; sample power, 10 mW) with the scattered photons directed into a single monochromator and focused onto a UV-sensitive liquid-N_2 cooled CCD detector (Horiba–Jobin Yvon CCD-3000V) with a spectral resolution of ∼2 cm^{-1} for the given parameters. The Raman spectrometer also was equipped with an environmentally controlled high-temperature environmental cell (Linkam, TS1500) that examined the catalyst samples in loose powder form (∼5–10 mg) and also allowed for control of both the temperature and gaseous composition. *In situ* Raman spectra were collected for the supported tungsten oxide catalysts after dehydration at 723 K for 1 h in flowing 10% O_2/He (Airgas, certified, 9.735% O_2/He, UHP and hydrocarbon-free, 30 mL/min) to desorb the adsorbed moisture, and the spectra of the dehydrated samples were collected after the catalysts were cooled to 393 K in flowing 10% O_2/He gas to ensure that the catalyst surface was devoid of moisture. Spectral acquisition was done with 20 scans of 20 s/scan, for a total acquisition time of ∼7 min per spectrum. System alignment was verified daily using a silica reference standard provided by Horiba–Jobin Yvon.

2.2.6. UV–vis diffuse reflectance spectroscopy

The electronic structures of the zirconia-supported tungsten oxide catalysts were obtained with a Varian Cary 5E UV–vis spectrophotometer using the integration sphere diffuse reflectance attachment (Harrick Praying Mantis Attachment, DRA-2). The finely ground powder catalyst samples (∼20 mg) were loaded into an *in situ* cell (Harrick, HVC-DR2) and measured in the 200–800 nm region using a magnesium oxide reflectance standard as the baseline. The UV–vis spectra of the supported tungsten oxide catalysts were obtained after the samples were treated at 673 K for 1 h in flowing 10% O_2/He (Airgas, certified, 9.735% O_2/He, UHP and hydrocarbon-free, 30 mL/min) to desorb the adsorbed moisture. Time-resolved *in situ* methanol dehydration studies were also carried out with reactor feed compositions of 6:12:82% CH_3OH/O_2/He and 6:94% CH_3OH/He at a total flow of 50 mL/min to study the effect of reduced sites at a reaction temperature of 573 K. Below 300 nm, the absorbance signal was unacceptably noisy, and thus a filter (Varian, 1.5ABS) was used to minimize the background noise.

The UV–vis spectra were processed with Microsoft Excel software, consisting of the calculation of the Kubelka–Munk function, $F(R_\infty)$ which was extracted from the UV–vis DRS absorbance. The edge energy (E_g) for the allowed transitions was determined by finding the intercept of the straight line in the low-energy rise of a plot of $[F(R_\infty)h\nu]^{1/n}$, where $n = 0.5$ for the direct allowed transition versus the incident photon energy, $h\nu$ [42–44].

2.2.7. Transmission electron microscopy

Samples for bright field (BF) and high-resolution (HR) transmission electron microscopy (TEM) examination were prepared by grinding and dispersing the catalyst powder in high-purity ethanol, then allowing a drop of the suspension to evaporate on a lacy carbon film supported by a 300-mesh copper TEM grid. "Dry" samples also were prepared for comparative purposes by dipping the TEM grid into the dry catalyst powder and then shaking off any loosely bound residue. BF-TEM images of the samples after exposure to ambient conditions were obtained using a JEOL 2000FX device operating at 200 kV. HR-TEM images of the samples were obtained using a JEOL 2200FS instrument with an accelerating voltage of 200 kV, a point-to-point resolution of 0.19 nm, and an information limit of 0.11 nm. Chemical analyses by X-ray energy dispersive spectroscopy (XEDS) were carried out using a dedicated VG HB603 STEM equipped with a Nion aberration corrector.

2.3. Reactivity studies

2.3.1. Methanol temperature-programmed surface reaction spectroscopy

Methanol temperature-programmed surface reaction (TPSR) spectroscopy was performed on an Altamira Instruments AMI-200 temperature-programmed system linked by a capillary tube to an online quadrupole mass spectrometer (Dycor Dy-Maxion DME200MS; Ametek Process Instruments). Typically, ∼100 mg of catalyst was loaded in a U-type quartz tube and initially pretreated in flowing air at 723 K (Airgas, Ultra-Zero-Grade Air, 30 mL/min) for 40 min to remove any possible adsorbed organic impurities and to dehydrate the sample. To ensure that the surface WO_x species remained in a fully oxidized state, the pretreated samples were initially cooled to 383 K, at which point the gas stream was switched to helium (Airgas, UHP, 30 mL/min) to flush out any residual gas-phase O_2. The sample was further cooled to 373 K and held for 30 min to remove any physically adsorbed O_2 and background gases. At 373 K, methanol adsorption was performed by flowing 2000 ppm CH_3OH/He (Airgas, 30 mL/min) for 30 min, after which the system was purged with flowing helium (Airgas, UHP, 30 mL/min) for another 30 min to remove any residual physically adsorbed methanol. Afterward, the sample was heated at a constant heating rate (10 K/min) to 773 K in flowing helium (Airgas, UHP, 30 mL/min). The gases exiting from the quartz tube reactor were analyzed with the online mass spectrometer as a function of catalyst temperature. The following m/e ratios were used for the identification of the various desorption gases: CH_3OH, $m/e = 31$; H_2CO, $m/e = 30$; CH_3OCH_3, $m/e = 45$ and 15 (DME); CO, $m/e = 28$; CO_2, $m/e = 44$; H_2O, $m/e = 18$; H_3COOCH, $m/e = 60$ (MF); and $(CH_3O)_2CH_2$, $m/e = 75$ (DMM). For those desorbing molecules that gave rise to several fragments in the mass spectrometer, additional m/e values also were collected to further confirm their identity. Recent studies demonstrated that the rate-determining step in methanol dehydration involves the first-order process that breaks the C–O bond in the surface CH_3O^* intermediate [45]. In addition, because the supported WO_x-zirconia samples are 100% acidic, forming only dimethyl ether (DME) as a product, the area under the DME/CH_3OH-TPSR curve corresponds to the number of exposed surface acid sites (N_s). By definition, N_s is equal to $\rho_{\mathrm{W,surf}}$ (W/nm^2) until monolayer coverage is reached, because the WO_x surface species are 100% dispersed in the sub-monolayer region. Above monolayer coverage, however, N_s was calculated from the following relationship:

$$N_s = \frac{\mathrm{ML}\rho_{\mathrm{W,surf}} \times \mathrm{AboveMLDesorptionArea}}{\mathrm{MLDesorptionArea}}. \tag{4}$$

2.3.2. Steady-state methanol dehydrogenation to dimethyl ether

Steady-state methanol dehydration experiments were conducted in an ambient pressure reactor consisting of a single-pass downflow fixed-bed quartz reactor (0.16″ ID) packed with finely ground catalyst powder and quartz endcaps. Catalyst loadings of 5–30 mg were chosen to maintain total methanol conversion under 10%, permitting the assumption of differential (i.e., gradientless) reactor conditions. To mimic thermal resistance and estimate catalyst bed temperature, a thermocouple mounted at the same elevation as the catalyst bed was installed inside an identical quartz tube that was fixed to the reactor tube. Both tubes were mounted side-by-side snugly within a 0.5″ ID metal tube wrapped in heat tape and insulation. Pretreatment consisted of calcining each catalyst at 623 K for 30 min in a 94 mL/min dry flowing gas mixture of oxygen (UHP, Airgas) and helium (UHP, Airgas) controlled at a molar O_2-to-He ratio of 14:79 by two independent Coriolis mass flow controllers. The reactor was then cooled to 573 K, after which the feed gases were bubbled through a liquid methanol saturator (Alfa Aesar, ACS grade). The gas-phase methanol concentration was controlled by the temperature of an overhead condenser, operated at 281 K for these experiments. The final composition of the reactor feed stream was 6:12:82% CH_3OH/O_2/He at 100 mL/min total flow (ST = 273.15 K, 101,325 N/m^2). Steady-state performance was determined by averaging 3–4 gas chromatography (GC) cycles at 573 K, and comparing this value to those of the initial runs at 373 K, where each catalyst was consistently demonstrated to be inactive in converting methanol. Blank runs without the catalysts demonstrated negligible methanol conversion in the reactor system. The 0.25″ OD stainless steel tubing from the reactor outlet to the GC was maintained at 393–423 K by heat tape and insulation, to minimize condensation of the reactor effluents. The reactor effluent gases were analyzed by an Hewlett Packard HP5890 Series II online gas chromatograph, operated in split mode (308 K for 6 min, ramp 20 K/min to 498 K hold for 5 min), with a 10-port Valco valve diverting two samples in parallel through a CP-sil 5CB capillary column (30 m × 0.32 mm × 5.0 µm; J&W Scientific) to a flame ionization detector and a 40/60 Carboxene-1000 packed column (5 ft × 1/8″, Supelco) to a thermal conductivity detector for determination of the methanol conversion, selectivity, and activity.

The steady-state methanol dehydration catalytic data are expressed in terms of turnover frequency (TOF; number of DME molecules formed/surface acid site/s) and turnover rate (TOR; number of DME molecules formed/total W-atoms/s). For the supported tungsten oxide catalysts below monolayer coverage, the number of surface acid sites was taken to be the number of surface WO_x species, which assumed 100% dispersion; this was independently confirmed with XPS and Raman spectroscopy. Above monolayer surface tungsten oxide coverage, the number of exposed surface acid sites was determined by the area under the DME/CH_3OH-TPSR curves and normalized to the value for monolayer coverage.

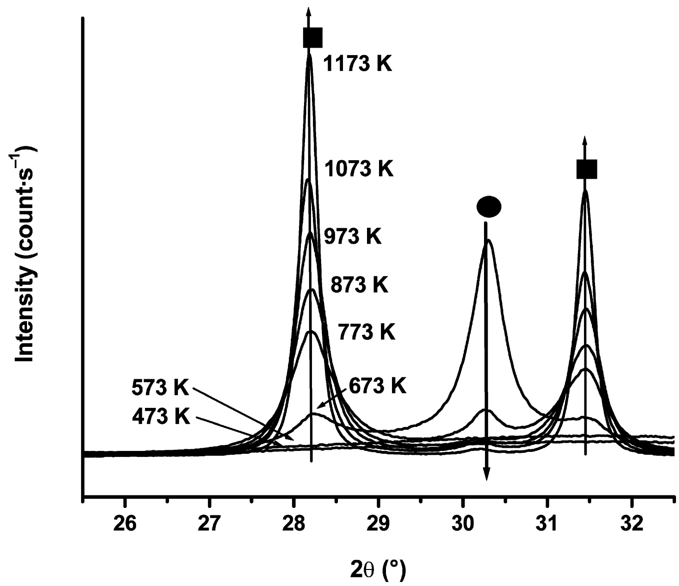

Fig. 1. Powder X-ray diffraction patterns of zirconium oxyhydroxide ($ZrO_x(OH)_{4-2x}$) calcined at different temperatures (absolute count rates for samples of constant volume). XRD-detectable ZrO_2 crystalline phases are marked as (■) m-ZrO_2 and (●) t-ZrO_2. Downward arrow indicates depletion of t-ZrO_2 phase with increasing calcination temperature.

3. Result

3.1. Catalyst characterization

3.1.1. BET surface area

The BET surface area values for the supported WO_3/ZrO_x-$(OH)_{4-2x}$ catalysts as a function of WO_x concentration and calcination temperature are given in Table 1. All of the trends observed with tungsten oxide loading and calcination temperature are consistent with those reported in the literature [20,25,46]. Increasing the calcination temperature at a constant WO_x loading led to a continuous decrease in the BET surface area as the underlying amorphous zirconia support sinters, crystallizes, and undergoes significant pore collapse; however, the BET surface area went through a maximum as a function of WO_x loading at a constant calcination temperature, which can be attributed to the surface stabilization of the ZrO_2 support by direct interaction with the surface WO_x species. It is important to note that multiple samples with different WO_x loadings and calcination temperatures can have similar $\rho_{W,surf}$ values for selected experimental conditions.

3.1.2. XRD

The XRD patterns for the WO_x-free zirconium oxyhydroxide support as a function of calcination temperature from 473 to 1173 K are shown in Fig. 1. The native $ZrO_x(OH)_{4-2x}$ support remained XRD-amorphous at calcination temperatures up to 573 K and crystallized to both the tetragonal-ZrO_2 (t-ZrO_2) and monoclinic-ZrO_2 (m-ZrO_2) polymorphs at higher temperatures. The volume fraction of t-ZrO_2 reached its maximum at 673 K, which is generally consistent with the previously reported behavior of hydrous zirconium oxide gels prepared at basic pH [47,48]. Higher calcination temperatures rapidly transformed the metastable t-ZrO_2 polymorph to the thermodynamically stable m-ZrO_2 polymorph. The t-ZrO_2 phase was almost completely transformed to the m-ZrO_2 polymorph at 1173 K.

The XRD patterns for all supported WZrOH catalysts also were consistent with previously reported trends [18,25,46]. For calcination temperatures ⩾773 K, every sample had some fraction of t-ZrO_2, and most had at least a trace of m-ZrO_2. The volume fraction of the m-ZrO_2 phase in the supported WZrOH materials (balance t-ZrO_2) as a function of WO_x content and calcination temperature is presented in Fig. 2. At the lowest calcination temperatures (773–873 K), m-ZrO_2 was not present in the catalyst samples with the highest WO_x loading, due to the structure-stabilizing effect of highly dispersed surface tungstate species. The volume fraction of m-ZrO_2 increased with decreasing WO_x loading at a constant temperature, providing further evidence of the stabilizing effect of surface WO_x. As would be expected based on thermodynamic considerations, increasing the calcination temperature at a constant WO_x concentration increased the m-ZrO_2 volume fraction.

3.1.3. XPS

The XPS surface W/Zr atomic ratios of the model supported $WZrO_2$ and supported WZrOH catalytic systems are shown in Fig. 3 as functions of surface W-atoms/nm^2 density. For the model supported $WZrO_2$ catalyst system (represented by the solid curve), the surface W/Zr ratio is linear up to $\rho_{W,surf} \sim 4.5$ W-atoms/nm^2 with an excellent least squares fit ($R^2 = 0.994$). Above 4.5 W-atoms/nm^2, the data points fall below the line, and the slope of the curve becomes very shallow due to the onset of crystalline WO_3 nanoparticles with diameters larger than the escape depth of excited electrons from the W(4f) transition (∼2.63 nm) [49–51]; consequently, the W(4f)

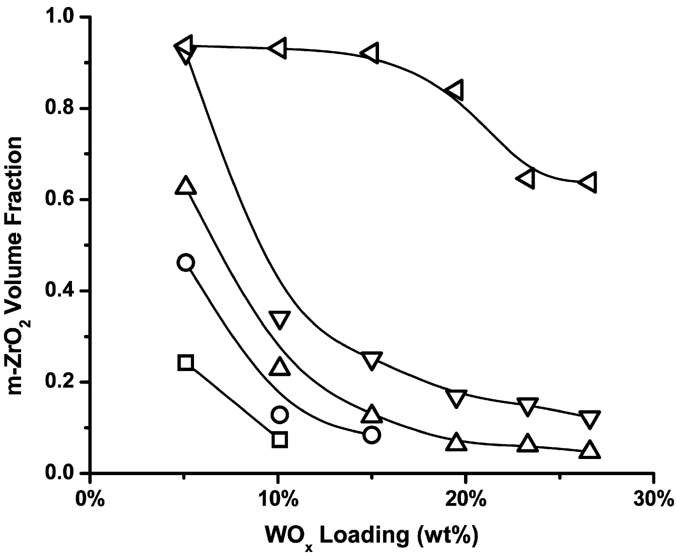

Fig. 2. Volume fraction of XRD-detectable crystalline ZrO_2 as m-ZrO_2 (balance t-ZrO_2) in WZrOH materials as a function of WO_x surface loading and calcination temperature: 773 K (□), 873 K (○), 973 K (△), 1073 K (▽), 1173 K (◁).

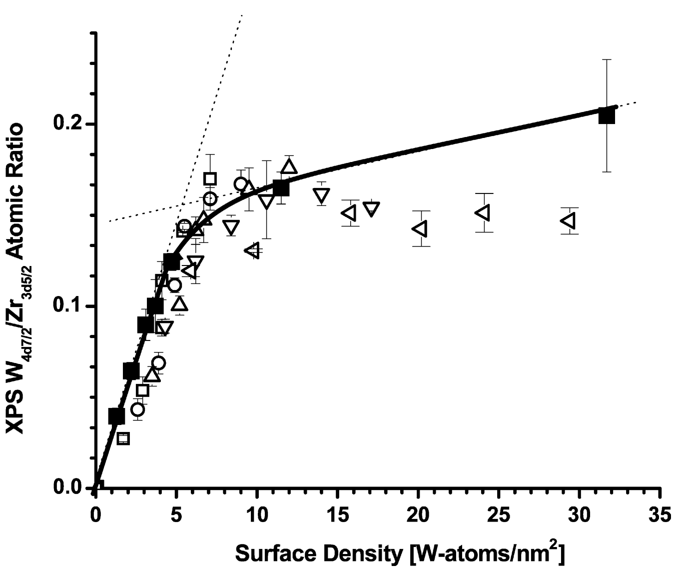

Fig. 3. XPS surface W/Zr atomic ratios of vacuum dehydrated samples determined from area integration and sensitivity factor correction for W $4f_{7/2}$ and Zr $3d_{5/2}$. Sample series include "model" supported xWZrO_2-723 (■) and supported xWZrOH-773 (□), -873 (○), -973 (△), -1073 (▽), -1173 K (◁).

electrons are not being collected from the entire supported WO_x phase or from the underlying ZrO_2 support. The determined onset point of WO_3 crystallite formation on WZrO_2 agrees with previous experimental XPS and ISS surface studies of model supported tungsten oxide catalysts [23,46,49,52,63,72].

The XPS surface W/Zr atomic ratios for the supported WZrOH catalyst samples are also presented in Fig. 3 (open symbols) as a function of surface W-atoms/nm^2 density and calcination temperature. Qualitatively similar to the model supported WZrO_2 materials, the surface W/Zr ratio for each of the supported WZrOH series at constant calcination temperature increases linearly at low WO_x loading, then exhibits a plateau

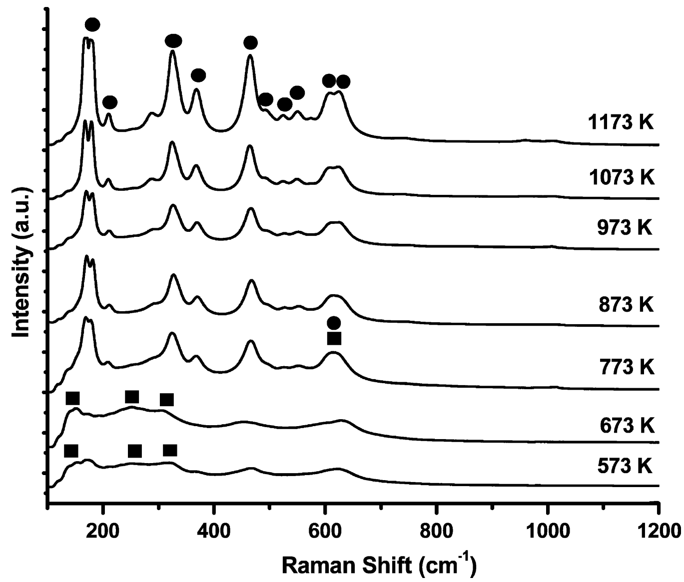

Fig. 4. Raman spectra (532 nm) under dehydrated conditions of $ZrO_x(OH)_{4-2x}$ materials as a function of calcination temperature (K) with bands that are unambiguously assigned as (■) t-ZrO_2 and (●) m-ZrO_2.

or even a negative deviation at higher WO_x concentrations. The negative deviation for the supported WZrOH materials at low and high tungsten oxide loadings suggests that the surface region also contains some extra ZrO_2 not present in the model supported WZrO_2 system. Assuming that the deviation from linearity for the WZrOH catalysts is due to WO_3 formation, the $\rho_{W,surf}$ at which the XPS W/Zr ratio deviates from linearity occurs at ∼5 W-atoms/nm^2.

3.1.4. Raman spectroscopy

3.1.4.1. Zirconia support Raman spectroscopy provided unique molecular structural insights into both the amorphous and crystalline ZrO_2 phases. Although both crystalline t-ZrO_2 and m-ZrO_2 phases share strong overlapping bands at 476 and 637–647 cm^{-1} [53,54], they also have additional unique vibrations at lower wavenumber values that allow discrimination between these two crystalline ZrO_2 phases. The m-ZrO_2 phase exhibits Raman bands at 180(s), 192(s), 220(w), 308(w), 335(m), 349(m), 383(m), 476(s), 503(w), 539(w), 561(w), 617(m), 638(m), and 756(w) cm^{-1}, whereas the Raman spectrum of the t-ZrO_2 phase contains bands at 149(m), 263–272(s), 290(w), 319(m), 412–423(w), 464(m), 476(s), 577(w), and 647(w) cm^{-1} [25,53,54].

The Raman spectra for WO_x-free zirconium oxyhydroxide as a function of calcination temperature, depicted in Fig. 4, are consistent with the XRD findings. The Raman bands for the 573–673 K calcined samples are very broad and characteristic of mostly amorphous materials; however, characteristic Raman vibrations due to crystalline t-ZrO_2 and m-ZrO_2, which cannot be detected by XRD, also are present. The highest concentrations of t-ZrO_2 are found at 573–673 K, and at increasing calcination temperature, loss of the Raman band at ∼153 cm^{-1} reflects progress of the phase transformation of t-ZrO_2 to m-ZrO_2 through the growth of the doublet at ∼179 and ∼208 cm^{-1} in

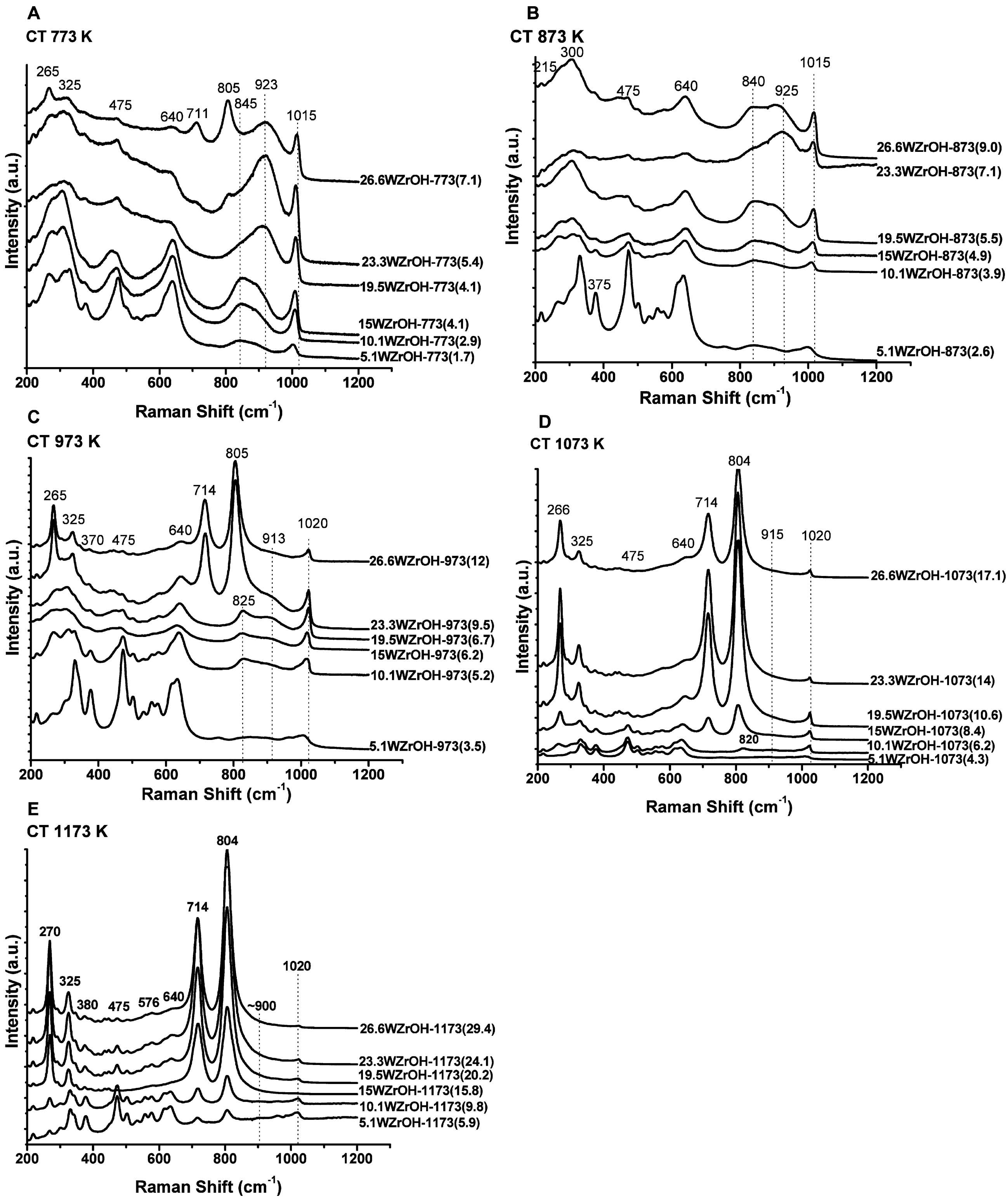

Fig. 5. Raman spectra (532 nm) under dehydrated conditions as a function of calcination temperature (K) and surface tungsten oxide coverage (W-atoms/nm^2) of supported tungsten oxide on the $ZrO_x(OH)_{4-2x}$ support: (A) CT 773 K, (B) CT 873 K, (C) CT 973 K, (D) CT 1073 K, and (E) CT 1173 K.

the Raman spectra, as well as the strong and medium bands at ~325 and ~367 cm^{-1}, respectively.

3.1.4.2. Supported $WO_3/ZrO_x(OH)_{4-2x}$ catalysts The Raman spectra of the supported $WO_3/ZrO_x(OH)_{4-2x}$ catalysts under dehydrated conditions are shown in Fig. 5. The supported $WO_3/ZrO_x(OH)_{4-2x}$ Raman spectra do not contain the features of crystalline $Zr(WO_4)_2$ [Raman features at 1028(s), 968(m), 931(s), 904(s), 860(m), 790(s), 734(s), 473(w), 378(s), 330(s), 305(m), 231(m), 175(w), 187(w), and 138(s) cm^{-1}] [55], Keggin $[XW_{12}O_{40}]^{3-}$ heteropolyacids [Raman features at 950–1015 cm^{-1} (ν_s(W=O)), 825–930 cm^{-1} (ν_{as}(W=O)), ~504–734 cm^{-1} (bridging W–O–W), and 149–450 cm^{-1} (δ(W–O–W))] [58], Wells–Dawson α-$[X_2W_{18}O_{62}]^{6-}$ heteropoly anions, and Wells–Dawson α_2-$[X_2W_{17}O_{61}]^{10-}$ lacunary species [multiple Raman W=O vibrations between 950–1005 cm^{-1} reflecting a distribution of distortions among the WO_6 units in the framework, as well as vibrations at ~500–700 cm^{-1} (bridging W–O–W) and 129–380 cm^{-1} (δ(W–O–W))] [55]. But the Raman features of crystalline m-WO_3 (133(s), 178(w), 187(w), 272(s), 327(m), 417(w), 437(w), 448(w), 715(s), and 805(s) cm^{-1}) [59–62] are present for high tungsten oxide $\rho_{W,surf}$ values and high calcination temperatures. The Raman spectra of the tungsten oxide component are generally found in the 700–1200 cm^{-1} region, because the strong crystalline ZrO_2 support vibrations tend to dominate the spectra below 700 cm^{-1} [31,36].

The Raman spectra in the 100–700 cm^{-1} region of Fig. 5 reveal that the crystallization of the zirconia support is strongly affected by both the supported tungsten oxide phase and the calcination temperature. At low $\rho_{W,surf}$ values, the zirconia support gives rise to well-defined m-ZrO_2 Raman bands. As the $\rho_{W,surf}$ value increases, the zirconia Raman bands broadens, reflecting the presence of smaller crystallites or less-ordered ZrO_2 particles, due to the retardation of zirconia crystallization by the supported tungsten oxide phase. At the highest $\rho_{W,surf}$ and modest calcination temperatures, the zirconia support Raman features are extremely weak and broad, reflecting the presence of an amorphous zirconia phase. Comparing the Raman spectra of W-free ZrO_2 and supported $WO_3/ZrO_x(OH)_{4-2x}$ shown in Figs. 4 and 5, respectively, at the same calcination temperature further emphasizes the retarding influence of the supported tungsten oxide phase on the crystallization of the ZrO_2 phase. Increasing the calcination temperature accelerates the crystallization of the zirconia support and tends to give rise to sharper ZrO_2 bands.

The Raman spectra in Fig. 5 also contain molecular structural information about the supported tungsten oxide phase in the 700–1200 cm^{-1} region. All of the dehydrated supported WZrOH catalyst samples exhibit a Raman band at ~1001–1020 cm^{-1} characteristic of dehydrated mono-oxo surface WO_5 monotungstate and mono-oxo surface WO_5/WO_6 polytungstate species, respectively [38,39,55]. The shift of the terminal mono-oxo W=O band from 1001 to 1020 cm^{-1} reflects the growing surface polytungstate domains with increasing $\rho_{W,surf}$ [55].

The onset of WO_3 crystallization is reflected by the presence of strong Raman bands at ~805, ~715, and ~270 cm^{-1} that increase in intensity with both $\rho_{W,surf}$ and calcination temperature. The onset of crystalline WO_3 formation at the different calcination temperatures occurs at $\rho_{W,surf} \geqslant 5.4$ W-atoms/nm^2 at 773 K (Fig. 5A), crystalline WO_3 is not present at 873 K (Fig. 5B), $\rho_{W,surf} > 6.7$ W-atoms/nm^2 at 973 K (Fig. 5C), $\rho_{W,surf} > 6.2$ W-atoms/nm^2 at 1073 K (Fig. 5D), and crystalline WO_3 is present at all surface densities investigated at 1173 K (Fig. 5E). The supported WZrOH catalyst samples also exhibit broad Raman bands in the ~820–850 cm^{-1} region that

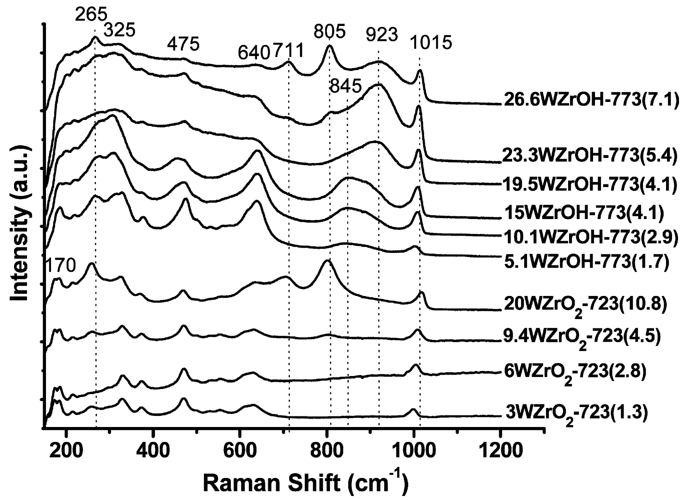

Fig. 6. Comparison of Raman spectra (532 nm) under dehydrated conditions as a function of surface tungsten oxide coverage (W-atoms/nm^2) of supported $WZrO_2$-723 and WZrOH-773 catalysts.

shift from ~850 to ~820 cm^{-1} with increasing tungsten oxide loading and calcination temperature. A similar effect is observed from ~900 to 925 cm^{-1}, as we elaborate on below.

3.1.4.3. Amorphous WO_3 phases The major difference between the Raman spectra of the supported WZrOH and the model supported $WZrO_2$ catalytic materials is the presence of the broad bands in the ~820–850 cm^{-1} and ~900–925 cm^{-1} regions for the supported WZrOH system, as shown in Fig. 6 [37,38]. The very broad nature of these Raman bands suggests that they may be associated with poorly ordered NPs. To investigate this possibility, the crystallization of amorphous WO_3 in the presence and absence of a minor amount of $ZrO_x(OH)_{4-2x}$ was examined. Amorphous WO_3 readily undergoes crystallization to well-ordered WO_3 with sharp Raman bands at relatively mild calcination temperatures (>673 K), as shown in Fig. 7A. Interestingly, weak vibrations in the 970–1020 cm^{-1} region are also present in the Raman spectra from some surface WO_x species on this bulk tungsten oxide material with a relatively higher surface area. The addition of a small amount of $ZrO_x(OH)_{4-2x}$, by aqueous impregnation onto the initial amorphous WO_3 material, dramatically retards the crystallization of the amorphous WO_3 phase, as shown in Fig. 7B. Even at very high calcination temperatures, the sharp characteristic Raman bands of crystalline WO_3 are still absent. An additional feature present in the $ZrO_x(OH)_{4-2x}/WO_3$ sample not found in the Zr-free WO_3 sample is a strong broad band in the 915–950 cm^{-1} region. Raman bands in the 915–950 cm^{-1} region are associated with bridging MO_x–O–Zr bonds [73], and such a weak band also has been detected for the model supported WO_3 catalysts [37,38]. Although the broad Raman bands in the 820–850 cm^{-1} region are not present for the calcined $ZrO_x(OH)_{4-2x}/WO_3$ sample, keep in mind that this sample consists of large tungsten oxide domains, whereas the supported WZrOH catalysts contain only small crystalline WO_3 particles. The slight shift of the crystalline WO_3 band from 805 cm^{-1} to ~820–850 cm^{-1}, along with the shift of this latter band from

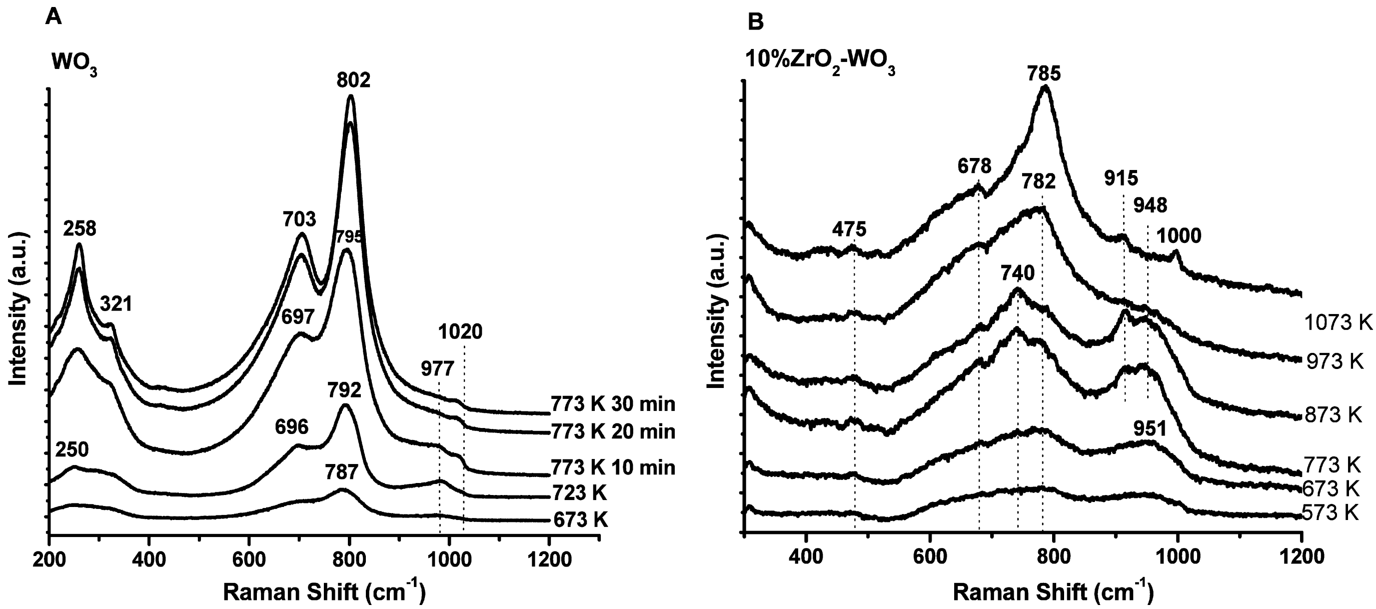

Fig. 7. Raman spectra (532 nm) of initially amorphous (A) WO_3 and (B) 10% ZrO_x–WO_3 mixture as a function of calcination temperature.

~850 to 820 cm^{-1} with increasing $\rho_{W,surf}$ and calcination temperature, suggest that the bands at ~820–850 cm^{-1} arise from distorted or poorly ordered WO_3 NPs that become more ordered or crystalline with increases in $\rho_{W,surf}$ and calcination temperature. Thus, the additional bands present in the Raman spectra of the supported WZrOH catalysts at ~820–850 and 900–925 cm^{-1} are related to Zr-stabilized distorted WO_3 NPs (Zr-WO_3).

3.1.4.4. Raman summary In summary, four different tungsten oxide structures were found to be present in supported WZrOH catalysts under dehydrated conditions: isolated surface mono-oxo W=O species (~1000 cm^{-1}), polymeric surface mono-oxo W=O species (~1020 cm^{-1}), distorted Zr-WO_3 NPs (~820–850 cm^{-1} and ~900–925 cm^{-1}), and well-ordered crystalline WO_3 NPs (~805, ~715, and ~270 cm^{-1}).

3.1.5. UV–vis DRS

3.1.5.1. Dehydrated conditions The UV–vis DRS E_g values for the dehydrated supported $WO_3/ZrO_x(OH)_{4-2x}$ (open symbols) and the model supported WO_3/ZrO_2 (closed symbols) catalyst systems are presented in Fig. 8 as a function of $\rho_{W,surf}$ and calcination temperature. For the well-defined model supported $WZrO_2$ samples in the sub-monolayer region (<4.5 W-atoms/nm^2), the E_g value drops from 5.2 to 4.2 eV with increasing surface tungsten oxide coverage. The corresponding ligand-to-metal charge transfer (LMCT) band maxima are observed at 218–219 and 240–246 nm, with a shoulder at 250–268 nm [55]. The E_g values and corresponding LMCT transitions of bulk tungstate reference compounds indicate that this value of 5.2 eV corresponds to monotungstate WO_x structures, and the value of 4.2 eV corresponds to a mixture of mono-tungstate and polytungstate WO_x structures [55]. The decrease in E_g values with increasing $\rho_{W,surf}$ up to monolayer coverage (4.5 W/nm^2) in the model supported $WZrO_2$ system reflects the fact that the surface WO_x species are becoming polymerized, with the extent of polymerization increasing very rapidly in the low-$\rho_{W,surf}$ region [58]. In the second region, between 4.5 and 10 W-atoms/nm^2, the E_g value continues to decrease with increasing tungsten oxide loading from 4.2 to 3.8 eV due to the presence of crystalline WO_3 NPs above monolayer coverage (see the Raman spectra in Fig. 6) [37,38]. Above 10 W-atoms/nm^2, the E_g value remains relatively constant with increasing $\rho_{W,surf}$, because large crystalline WO_3 particles are present, and the E_g value effectively approaches that of bulk WO_3 crystals.

The UV–vis DRS E_g values for the supported WZrOH series track the same E_g value trend of the model supported $WZrO_2$ series in the sub-monolayer region up to ~4.5 W/nm^2 regardless of calcination temperature. The corresponding LMCT band maxima occurs at ~250 nm for all of the supported WZrOH catalysts, which is characteristic of highly distorted mono-tungstate and polytungstate WO_x structures [55]. An additional LMCT band at ~230 nm from regular monotungstate WO_x species [55] is observed only for the 5.1WZrOH-873(2.6), 10.1WZrOH-873(3.9), and 5.1WZrOH-1173(5.9) catalyst samples. This decreasing trend in E_g value at low $\rho_{W,surf}$ values reflects the enhanced electron delocalization with increasing domain size of surface WO_x species in going from isolated to polymeric structures. The overlapping E_g values for the two catalyst series suggests that the electronic structure of the surface WO_x species is generally similar for both supported WZrOH and $WZrO_2$ catalyst systems in this region. For higher $\rho_{W,surf}$, the E_g value for the supported WZrOH series further decreases from ~4.2 to 4.0 eV until ~10 W-atoms/nm^2 is attained and then remains constant at this value for all high surface W-atoms/nm^2 density. The further decrease in E_g value from ~5–10 W-atoms/nm^2 reflects the presence of WO_3 3D nanodomains (as confirmed by the Raman spectra in Fig. 5). A striking difference between the supported WZrOH and $WZrO_2$ series is the slightly higher E_g values for the WZrOH system above ~4.5 W-atoms/nm^2. This higher

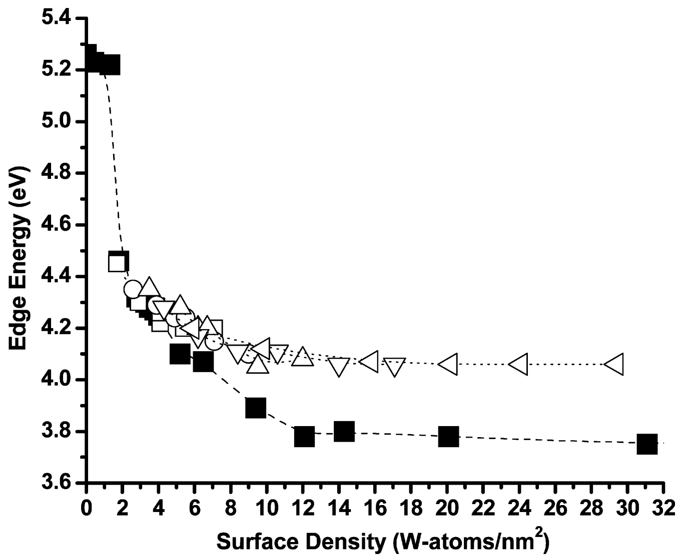

Fig. 8. UV–vis DRS edge energy, E_g (eV), for supported WO_3 catalysts as a function of surface density (W-atoms/nm^2) for "model" xWZrO$_2$-723 (■) and xWZrOH-773 (□), -873 (○), -973 (△), -1073 (▽), -1173 (◁).

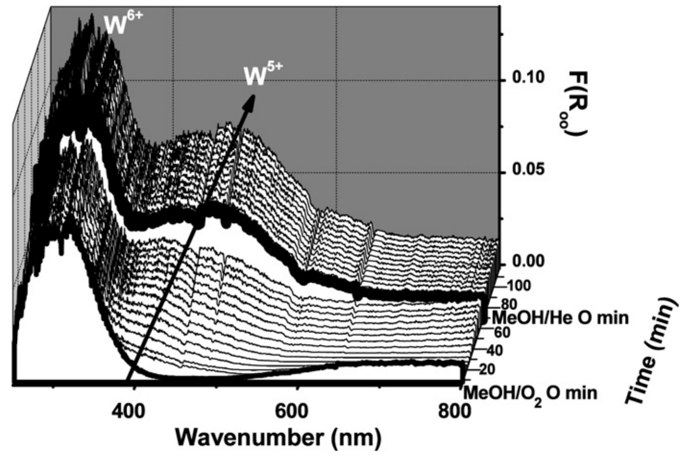

Fig. 9. *In situ* time-resolved UV–vis spectra at 573 K in CH_3OH/O_2 and CH_3OH/He environments for the 15WZrOH-973(6.2) catalyst sample.

E_g value for the supported WZrOH catalysts is attributed to the presence of the smaller Zr-stabilized distorted WO_3 NPs (Zr-WO_3) that are not present in the model $WZrO_2$ catalysts. Furthermore, the constant E_g value of ~4.0 eV above ~10 W-atoms/nm^2 reflects the fact that large bulk-like WO_3 crystallites are not present for the supported WZrOH system, in direct contrast to the supported $WZrO_2$ system in this $\rho_{W,surf}$ region.

3.1.5.2. Reaction conditions The time-resolved *in situ* UV–vis DRS spectra of the very active supported 15WZrOH-973(6.2) catalyst (see Section 3.2.2 below) under different reaction conditions at 573 K are presented in Fig. 9. UV–vis DRS can follow the oxygen LMCT bands for both the W^{6+} (~300–400 nm) and W^{5+} (~400–500 nm) cations. The absorption maximum at ~400–500 nm is attributed to d-d transitions of W^{5+} centers, in accordance with Barton et al. [22]. Under the reducing CH_3OH/He environment, the position of the W^{6+} band is minimally affected by the reducing CH_3OH/He environment, but the W^{5+} band is present with an upward shift in baseline over time. Under the more oxidizing environment of $CH_3OH/He/O_2$, only a slight reduction of the surface W^{6+} to W^{5+} occurs. No significant changes in the edge energy are seen, suggesting that formation of the reduced sites do not reflect changes in the W^{6+} domain size or structure, as described previously [22]. Simultaneous online product detection by mass spectrometry showed that DME production was exactly the same in the presence and absence of O_2 in the CH_3OH/He environment, suggesting that the reduced WO_x domains are not the catalytic active sites for methanol dehydration to DME.

3.1.5.3. UV–vis DRS summary In summary, the UV–vis DRS measurements reflect the presence of four distinct tungsten oxide structures in the supported WZrOH and $WZrO_2$ catalytic materials under dehydrated conditions: (i) isolated surface WO_x species at very low surface coverage; (ii) polymeric surface WO_x species at monolayer coverage; (iii) well-ordered WO_3 and distorted Zr-WO_3 NPs above monolayer coverage for $WZrO_2$ and WZrOH, respectively; and (iv) bulk-like crystalline WO_3 particles and Zr-stabilized WO_3 NPs above ~10 W-atoms/nm^2 for WZrOH. The distorted Zr-WO_3 NPs present for WZrOH catalysts consist of smaller domains than the well-ordered WO_3 NPs. Furthermore, reduced W^{5+} cations also are present under the reducing conditions of CH_3OH/He, and their presence is not related to DME formation.

3.1.6. TEM

3.1.6.1. Zirconia support Representative BF images of the supported WZrOH catalysts are shown in Fig. 10. The W-free $ZrO_x(OH)_{4-2x}$ support calcined at 773 K is depicted in Fig. 10A and consists of crystalline ZrO_2 particles showing some evidence of retained internal voids and/or surface pits (as represented by the 2–10 nm lighter regions). These features are presumably related to the loss of water from the $ZrO_x(OH)_{4-2x}$ material and sintering of the support. The support structure sinters to more condensed and larger m-ZrO_2 particles as the calcination temperature is further increased (not shown for brevity). BF images of selected supported WZrOH catalysts are presented in Figs. 10B–10F; these also predominately show ZrO_2 particles with the structure described previously, that is, mildly sintered at lower temperatures and more condensed at calcination temperatures above 1073 K. BF imaging demonstrated that the mean size of this majority type of ZrO_2 particles in the underlying support for this specific set of WZrOH catalysts increases progressively with calcination temperature as follows: <10 nm at 773 K, ~10 nm at 873 K, 10–15 nm at 973 K, ~20 nm at 1073 K and between 20 and 40 nm at 1173 K. All samples also occasionally exhibited highly condensed ZrO_2 particles of around 100–200 nm in diameter, which constituted a very minor volume fraction of the total support material. These larger particles were presumably formed by local inhomogeneities in the heating conditions. Comparing the W-free $ZrO_x(OH)_{4-2x}$-773 and 10.1WZrOH-773(2.9) catalyst samples reveals a considerably finer ZrO_2 crystalline grain structure for WZrOH-773 compared with the W-free $ZrO_x(OH)_{4-2x}$-

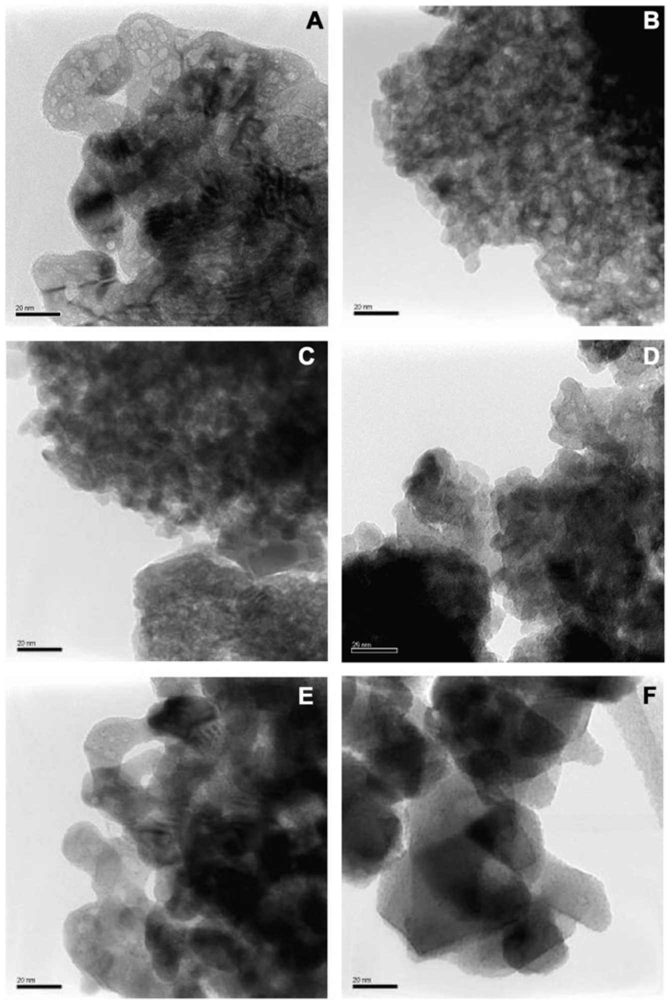

Fig. 10. Representative bright field (BF) images of supported tungsten oxide on the initial $ZrO_x(OH)_{4-2x}$ support: (A) W-free $ZrO_x(OH)_{4-2x}$-773, (B) 10.1WZrOH-773(2.9), (C) 19.5WZrOH-873(5.5), (D) 23.3WZrOH-973(9.5), (E) 10.1WZrOH-1073(6.2), and (F) 19.5WZrOH-1173(20.2).

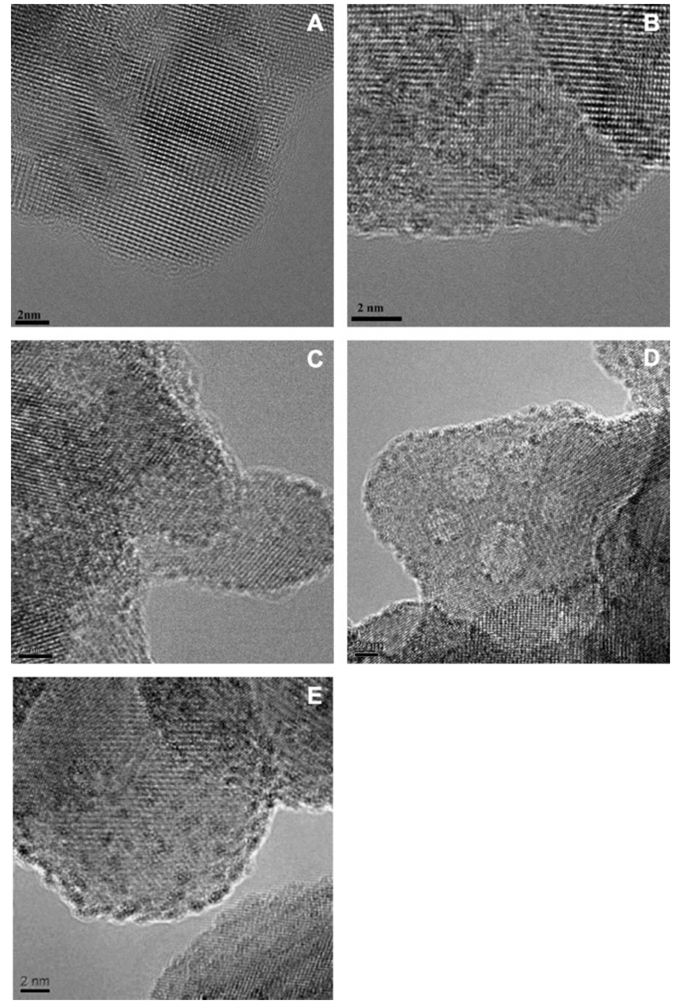

Fig. 11. Representative HR-TEM images of supported tungsten oxide on the initial $ZrO_x(OH)_{4-2x}$ support: (A) 10.1WZrOH-773(2.9), (B) 19.5WZrOH-873(5.5), (C) 23.3WZrOH-973(9.5), (D) 10.1WZrOH-1073(6.2), and (E) 19.5WZrOH-1173(20.2).

773. The smaller ZrO_2 particles present in WZrOH-773 are a direct consequence of the strong interaction between the WO_x species and the $ZrO_x(OH)_{4-2x}$ support during its crystallization. Internal voids within support grains were not found for the model supported $WZrO_2$ catalyst system, which consists of dense, coarse m-ZrO_2 particles with only some retained intergranular porosity [39].

3.1.6.2. Supported tungsten oxide domains The BF images in Figs. 10B–10F also contain ∼1-nm dark flecks that STEM-XEDS elemental analysis revealed to be rich in tungsten. These WO_x-containing domains are occasionally observed, especially by annular dark-field imaging, even at a very low $\rho_{W,surf} = 2.9$ W-atoms/nm^2 for the 10.1WZrOH-773(2.9) catalyst sample in which crystalline WO_3 is not present (according to the corresponding Raman spectra in Fig. 5). Similarly, these features also are found in the supported 19.5WZrOH-873(5.5) and 10.1WZrOH-1073(6.2) catalysts (Figs. 10C and 10E, respectively), in which crystalline WO_3 is not detected with Raman spectroscopy.

Representative HR-TEM images of the supported WZrOH catalysts are shown in Fig. 11 for selected supported WZrOH catalysts. The amorphous overlayer of surface WO_x species is visible when viewed in profile, with the small WO_x-rich domains observed (in Figs. 11B–11E) as darker flecks against the zirconia support due to their higher mass contrast. A general trend of increasing number density of the dark WO_x-rich specks with increasing W-atoms/nm^2 is seen. The smallest number density of WO_x-rich domains is present at the lowest calcination temperatures and $\rho_{W,surf}$, and the largest number density WO_x-rich domains is present at the higher calcination temperatures and $\rho_{W,surf}$. A gradual slight increase in the average fleck dimensions, irrespective of whether the TEM samples were prepared by the wet or dry route, also was noted in this particular series of samples (i.e. 873 K samples: 0.6–0.8 nm; 973 K samples: 0.8–0.9 nm; 1073 K samples: 0.7–1.1 nm; 1173 K samples: 1.0–1.3 nm). At low $\rho_{W,surf}$ values (<6 W-atoms/nm^2), the tungsten-rich domains most likely correspond to hydrated WO_x clusters (e.g., $H_6W_6O_{21}\cdot nH_2O$) [56] and possibly Zr-stabilized distorted WO_3 NPs that were de-

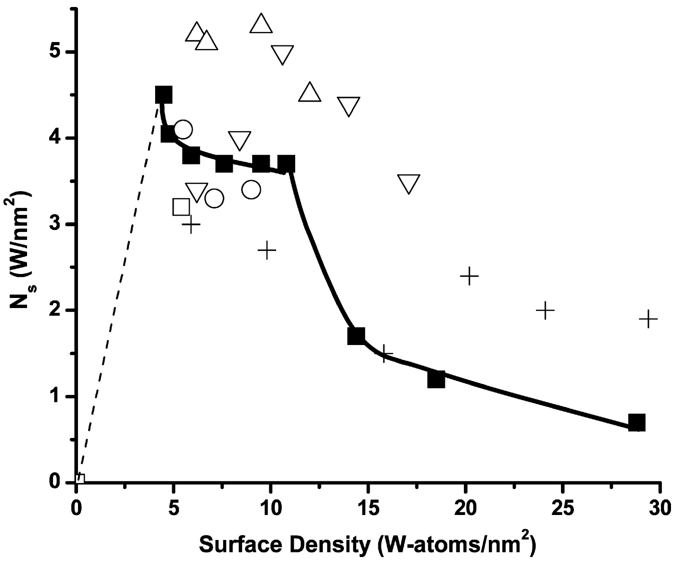

Fig. 12. Number of exposed W-sites/nm^2 for zirconia-supported tungsten oxide catalysts as a function of surface density (W-atoms/nm^2) for "model" xWZrO$_2$-723 (■) and xWZrOH-773 (□), -873 (○), -973 (△), -1073 (▽), -1173 (◁).

tected with Raman spectroscopy, because the signature resonances for well-ordered crystalline WO_3 particles are absent in the Raman spectra. At high $\rho_{W,surf}$ values (>6 W-atoms/nm^2), the tungsten-rich flecks most likely correspond to distorted Zr-WO_3 NPs and hydrated WO_x clusters. Corresponding SEM images revealed that large (2–6 µm) WO_3 crystals also are present in samples at ~8 W/nm^2 and higher surface tungsten oxide density values.

3.2. Reactivity studies

3.2.1. Methanol-TPSR and N_s determination

Methanol-TPSR dehydration studies were conducted to chemically probe the nature of the catalytic active sites present in the zirconia-supported tungsten oxide catalysts, because this reaction is known to proceed readily over surface acidic sites [59]. Unfortunately, the methanol dehydration reaction does not discriminate between Lewis and Brønsted acid sites, but does provide quantitative information about the number of exposed surface WO_x catalytic active sites, N_s, which is reflected in the area under the DME-TPSR product curve.

The determined N_s values are plotted in Fig. 12 for the supported WZrOH catalysts (open symbols) and compared with those of the model supported $WZrO_2$ catalysts (solid curve and closed symbols) as a function of $\rho_{W,surf}$. Measurements were not made below 4.5 W-atoms/nm^2, because exposed ZrO_x sites also are present in this region (dashed linear region). The linear increase in N_s from 0 to 4.5 W-atoms/nm^2 was simply taken from the number of W atoms in the catalyst, because, by definition, the surface WO_x species are 100% dispersed in the sub-monolayer region. Depending on calcination temperature and WO_x loading, either a gentle increase or decrease in N_s is observed in the 4.5–10 W-atoms/nm^2 range, with a significant decrease above 10 W-atoms/nm^2 for both the supported WZrOH and $WZrO_2$ catalyst series. The decrease in N_s above 10 W-atoms/nm^2 reflects the presence of less-dispersed and larger WO_3 crystallites that have fewer exposed sites than the dispersed surface WO_x phase. Compared with the model supported $WZrO_2$ series, the supported WZrOH series at higher calcination temperatures typically has higher N_s values, suggesting that a slightly greater number of catalytic active sites may be present for the supported WZrOH series than for the supported $WZrO_2$ series.

3.2.2. Steady-state methanol dehydration

Steady-state methanol dehydration studies were conducted to examine the surface acidic properties of the supported WZrOH catalysts. Every catalyst sample yielded 100% selectivity to dimethyl ether (DME), verifying the acidic nature of the supported WZrOH catalysts. Multiple samples were tested in both the presence and absence of a gaseous oxygen co-feed, and no appreciable difference in catalytic activity was observed when gaseous molecular O_2 was present or absent in the feed. This demonstrates that (i) the reaction is zero-order with respect to oxygen, (ii) a redox surface reaction mechanism does not occur, and (iii) partially reduced WO_x species are not the acidic catalytically active site for methanol dehydration under the test conditions (consistent with the UV–vis DRS measurements reported above). Consequently, the catalytic data presented in Fig. 13 were obtained with oxygen-containing feed streams.

3.2.2.1. Catalytic TOF results The catalytic TOF values for the supported WZrOH and $WZrO_2$ systems are plotted in Fig. 13A as a function of $\rho_{W,surf}$. The reaction rates were converted to TOF values using the N_s values determined from the CH_3OH-TPSR experiments and are shown in Fig. 13A. The resulting TOF curves for the model supported $WZrO_2$ and the supported WZrOH series differ significantly at the same $\rho_{W,surf}$ value, indicating that factors other than surface W-atoms/nm^2 significantly affect the TOF value. The TOF for the supported WZrOH catalysts increases monotonically to $\rho_{W,surf} \sim 6$ W-atoms/nm^2, then decreases with further increases in $\rho_{W,surf}$. The supported WZrOH catalysts calcined at 773 and 1173 K do not attain TOF values comparable to those of the supported WZrOH samples calcined at 873–1073 K and are an order of magnitude less active than the highest TOF achieved. But the supported WZrOH catalysts calcined at 773 and 1173 K still exhibit TOF values that are a factor of 10^1–10^2 greater than the those of the model supported $WZrO_2$ catalysts. Another interesting difference between the supported WZrOH and the model supported $WZrO_2$ catalyst system is that the TOF for the former system decreases above $\rho_{W,surf} \sim 6$ W-atoms/nm^2, whereas that for the latter continues to increase with increasing $\rho_{W,surf}$ above this level.

3.2.2.2. Catalytic TOR results The catalytic TOR values, presented in Fig. 13B, were determined by normalizing the catalytic activity by all of the W atoms in the catalyst whether present as surface WO_x species or as crystalline WO_3 NPs, with the latter clearly having dispersion significantly <100%. This overcounting of catalytically active sites decreases the TOR values at high $\rho_{W,surf}$ values and contributes to the maximum

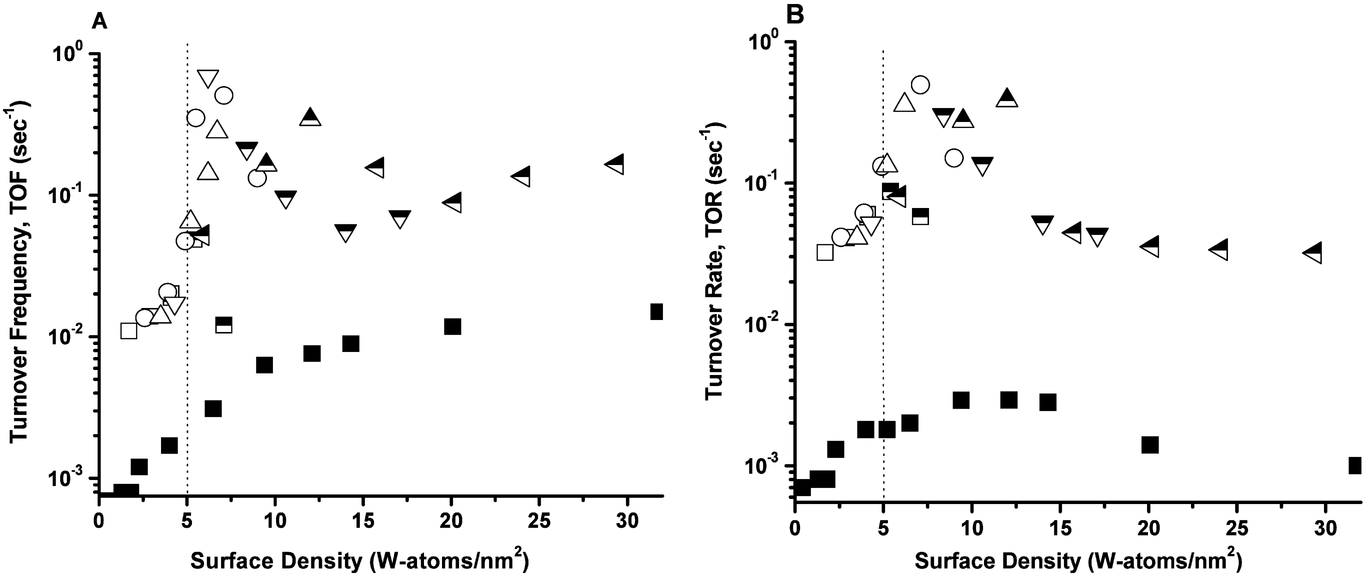

Fig. 13. Catalytic acidity for CH_3OH dehydration to DME over zirconia-supported tungsten oxide catalysts: (A) turnover frequency (TOF) as a function of surface density (W-atoms/nm^2) and (B) turnover rate (TOR) as a function of surface density (W-atoms/nm^2) for "model" xWZrO$_2$-723 (■) and xWZrOH-773 (□), -873 (○), -973 (△), -1073 (▽), -1173 (◁). The half-filled symbols for the supported WZrOH catalyst samples represent the detection of crystalline WO_3 NPs with Raman spectroscopy.

in TOR at intermediate $\rho_{W,surf}$ values. For example, the TOF plot for the model supported WZrO$_2$ series does not exhibit a maximum, but does have a maximum at ∼8 W-atoms/nm^2 when plotted as TOR. For the supported WZrOH series, the TOF maximum occurs at ∼6 and at ∼8 W-atoms/nm^2 for TOR. Thus, the maximum in TOR plots is an artificial maximum that is a consequence of overcounting the number of catalytically active sites. Nevertheless, the current acid-catalyzed CH_3OH dehydration studies corroborate previous studies using n-butanol dehydration, n-pentane isomerization, n-heptane isomerization, and o-xylene isomerization indicating that the acid catalysis for supported WO_x–ZrO_2 materials exhibits TOR maxima at intermediate $\rho_{W,surf}$ values [17–19,21,23]. In addition, the TOR values for the supported WZrOH series is about a factor of 10^2 greater than the TOR values for the model supported WZrO$_2$ series, which is in agreement with early observations by Hino and Arata [1].

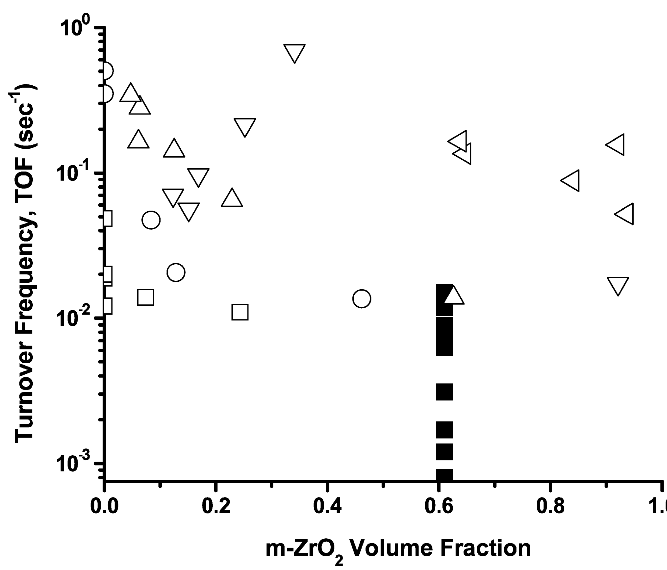

Fig. 14. Catalytic acidity, turnover frequency (TOF), for CH_3OH dehydration to DME over zirconia-supported tungsten oxide catalysts versus volume fraction of XRD-detectable crystalline ZrO_2 as m-ZrO$_2$ (balance t-ZrO$_2$) in zirconia-supported tungsten oxide catalysts for "model" xWZrO$_2$-723 (■) and xWZrOH-773 (□), -873 (○), -973 (△), -1073 (▽), -1173 (◁).

4. Discussion

4.1. Zirconia support

The W-free zirconium oxyhydroxide amorphous material is metastable and readily crystallizes to t-ZrO$_2$ and m-ZrO$_2$ phases at 673 K and above, with the thermodynamically more stable crystalline m-ZrO$_2$ phase dominating at higher temperatures. But the supported WZrOH catalyst system tends to crystallize as mixtures of t-ZrO$_2$ and m-ZrO$_2$. The t-ZrO$_2$ phase dominates for high $\rho_{W,surf}$ and more modest calcination temperatures (773–1073 K), whereas the m-ZrO$_2$ phase dominates for low $\rho_{W,surf}$ and especially high calcination temperatures. The morphology of the ZrO_2 particles also is affected by the presence of WO_x and results in smaller ZrO_2 crystallites with a higher BET surface area. The stabilization of the t-ZrO$_2$ phase and the formation of smaller ZrO_2 particles for the WZrOH catalyst samples are a direct consequence of the interaction of WO_x with the ZrOH substrate during its crystallization to ZrO_2.

The possible relationship between methanol dehydration catalytic activity of the supported WZrOH catalysts and the ZrO_2 crystalline phase composition is examined in Fig. 14, which plots the TOF against the m-ZrO$_2$ volume fraction, as determined from XRD measurements. For a wide range of m-ZrO$_2$ volume fractions, essentially the same TOF value is observed, suggesting that the specific ZrO_2 crystalline phase does not affect the TOF for methanol dehydration to DME over the supported WZrOH catalysts [60,61].

The metastable $ZrO_x(OH)_{4-2x}$ support also affects the crystallization of the initially amorphous WO_x component, because Zr-stabilized distorted WO_3 NPs are formed both below and above monolayer coverage (see Figs. 5 and 6). The distorted Zr-WO_3 NPs are not present when crystalline m-ZrO_2 is used as a support and are present only when metastable $ZrO_x(OH)_{4-2x}$ is used as the support. Thus, some of the metastable $ZrO_x(OH)_{4-2x}$ component is able to interact and intermix with the amorphous WO_x component during the crystallization process (see Fig. 7).

4.2. Monolayer surface WO_x coverage

Monolayer surface coverage for the supported WZrOH catalyst system deviates slightly from the strict definition of monolayer coverage, because some Zr-stabilized distorted WO_3 NPs also are present below monolayer coverage (see the Raman spectra in Figs. 5 and 6). Despite this minor difference, however, the XPS surface analysis of the supported WZrOH and model supported $WZrO_2$ catalysts demonstrate that comparable monolayer coverage of $\rho_{W,surf} \sim 4.5$–5 W-atoms/nm^2 is obtained for both catalytic systems regardless of the crystallographic form of the underlying support material (i.e., t-ZrO_2, m-ZrO_2, or their mixtures). For the supported WZrOH catalyst series, the XPS W/Zr ratios are slightly below those of the model supported $WZrO_2$ series, suggesting enrichment of Zr in the surface region at the low and high $\rho_{W,surf}$ values. Such Zr enrichment can result from smaller WO_3 NPs, especially the presence of smaller Zr-stabilized WO_3 NPs.

The experimental data reported for monolayer coverage of surface WO_x species is actually consistent among investigators. Previous XPS, ISS, CO-chemisorption, and Raman spectroscopy characterization of supported $WZrO_2$ by Vaidyanathan et al. [36,49] concluded that monolayer coverage of surface WO_x species corresponds to $\rho_{W,surf} \sim 4$ W-atoms/nm^2, and that crystalline WO_3 NPs also are present at higher $\rho_{W,surf}$ values. Using low-temperature IR spectroscopy with CO-chemisorption and tracing the disappearance of the surface Zr–OH vibrations and the effect of CO on the vibrations of the W=O stretching modes, Scheithauer et al. [17] also concluded that monolayer surface coverage for supported WZrOH corresponds to $\rho_{W,surf} \sim 4.0$–4.8 W-atoms/nm^2. Using Raman spectroscopy, Barton et al. [22] similarly found that the $\sim$805 cm^{-1} band for crystalline WO_3 NPs was absent for the catalyst samples with $\rho_{W,surf} < 5$ W/nm^2 but present at higher loadings and increased linearly with loading >5 W-atoms/nm^2. From CO_2-chemisorption in which the surface Zr–OH groups were titrated, Barton et al. also found that all the exposed surface Zr–OH exposed was titrated by the surface WO_x species when $\rho_{W,surf}$ approached $\sim$4.5 W-atoms/nm^2, which is consistent with monolayer coverage reported previously [22]. A similar chemical transition also was observed at $\rho_{W,surf} \sim 4.1$ W-atoms/nm^2 during H_2 reduction monitored by UV–vis [22]. The supported WO_x species on ZrO_2 was not reduced at <4.1 W-atoms/nm^2 but was reduced at >4.1 W-atoms/nm^2. It was proposed that only the samples at >4.1 W/nm^2 contained the W–O–W bonds needed to reduce the surface polytungstate and crystalline WO_3 domains [22]. The present study demonstrates that surface polytungstate species, with bridging W–O–Zr bonds, are present at <4.5 W-atoms/nm^2, and that crystalline WO_3 and distorted Zr-WO_3 NPs, primarily containing bridging W–O–W bonds, become dominant above monolayer coverage (>4.5 W-atoms/nm^2). Therefore, all of the *experimental* characterization studies reported the past three decades indicate that monolayer surface coverage for supported tungsten oxide catalysts on ZrO_2 corresponds to $\rho_{W,surf} \sim 4$–5 W-atoms/nm^2 and is independent of the type of oxide support (with the exception of inert SiO_2 support) [17,20,22,25,36,49,57,62–72].

The only differing monolayer surface WO_x coverage values reported in the literature correspond to *theoretical* estimates that are based on bulk structural assumptions of how a crystalline WO_3 lattice hypothetically would interact with the relatively perfect surface of crystalline ZrO_2. As is well known, and has been strikingly demonstrated above, the supported tungsten oxide phase and the ZrO_2 support structures cannot be represented by model crystalline WO_3 and crystalline ZrO_2 phases, respectively.

4.3. Nature of WO_x species in the sub-monolayer region (<5 W-atoms/nm^2)

The combined *in situ* UV–vis and Raman studies of the supported WZrOH catalysts indicate that the dehydrated surface WO_x species become progressively polymerized with surface tungsten oxide coverage in the sub-monolayer region. This is reflected by the decrease in the UV–vis E_g value from $\sim$4.5 to $\sim$4.0 eV due to polymerization of the surface WO_x species and the shift of the W=O Raman band from $\sim$1000 to $\sim$1020 cm^{-1}, corresponding to monotungstate and polytungstate surface $O_4W{=}O$ species, respectively [55]. The same dehydrated surface WO_x species as a function of surface coverage in the sub-monolayer region also are present for the model supported $WZrO_2$ catalysts, because both the UV–vis E_g values and Raman band positions vary in a similar manner as a function of $\rho_{W,surf}$ for both the supported WZrOH and supported $WZrO_2$ series up to monolayer coverage (see Figs. 5–7) [37,38].

There is only one significant difference between the supported WZrOH and model $WZrO_2$ catalyst series in the sub-monolayer region. The supported WZrOH catalysts also have some Zr-stabilized distorted WO_3 NPs (see the Raman spectra in Figs. 5 and 6). But the concentration of these distorted Zr-WO_3 clusters in the sub-monolayer region cannot be high, because the overall UV–vis E_g values are not significantly perturbed by their presence (compare the behavior of WZrOH and $WZrO_2$ in Fig. 8). Raman bands at $\sim$820 and 910–950 cm^{-1} corresponding to distorted Zr-WO_3 NPs also have been reported by Barton et al. and Knozinger et al. in the monolayer region [17,22,25]. The former group did not discuss these Raman bands; the latter group assigned them to possible Zr-WO_x heteropoly anions (HPAs), based on low-temperature CO chemisorption evidence of exposed Zr at high tungsten oxide coverage [17,25]. However, when silicotungstic acid HPA was impregnated onto the model supported $WZrO_2$ monolayer catalyst, it was found to decompose on calcination at 723 K, and also did not give rise to enhanced catalytic performance for methanol dehydration. Thus, the presence of distorted Zr-WO_3 NPs also was reported previously, but was not properly assigned.

Barton et al. found a relatively constant UV–vis E_g value of ~4 eV of <4 W-atoms/nm^2 for their supported WZrOH catalysts and assigned this value to isolated surface WO_x species [22]. But the UV–vis E_g value of ~4 eV corresponds to polytungstate reference compounds [55]. In the present study, the UV–vis E_g value for the supported WZrOH catalysts in the sub-monolayer region also was found to be relatively constant, ~4.2–4.3 eV, from 2.6 to 5 W-atoms/nm^2, but to increase dramatically, to ~5.2 eV, at lower $\rho_{W,surf}$ values. Furthermore, the same UV–vis E_g trend also is observed for the model supported $WZrO_2$ series, reflecting polymerization of the surface tungsten oxide species with coverage in the sub-monolayer region (see Fig. 8). Thus, surface WO_x species are present mostly as surface monotungstate species at ~1 W-atoms/nm^2 and as surface polytungstate species as monolayer coverage (~5 W-atoms/nm^2) is approached.

4.4. Nature of WO_x species above monolayer coverage

The two-dimensional surface WO_x monolayer coexists with three-dimensional WO_3 NPs above monolayer coverage for both the supported WZrOH and model $WZrO_2$ catalyst series. For the model supported $WZrO_2$ catalysts, the WO_3 NPs are present only as well-ordered WO_3 crystallites. For the supported WZrOH catalysts just above monolayer (5–8 W/nm^2), however, the WO_3 NPs are generally present as Zr-stabilized distorted WO_3 NPs at modest calcination temperatures. At higher $\rho_{W,surf}$ and calcination temperatures, well-ordered crystalline WO_3 NPs coexist with the distorted Zr-WO_3 NPs, as indicated by the higher UV–vis E_g values for the supported WZrOH series compared with those for the model supported $WZrO_2$ series (see Fig. 8).

4.5. Determination of catalytic active sites for supported WZrOH catalysts

The only substantial difference between the model supported $WZrO_2$ and WZrOH catalysts in the sub-monolayer region is the presence of the Zr-stabilized distorted WO_3 NPs for the supported WZrOH catalysts, as depicted in Scheme 1 (see Fig. 6). Thus, the enhancement of acidic TOF/TOR activity by a factor of 10^1–10^2 for the supported WZrOH catalysts must be due to the presence of the distorted Zr-WO_3 NPs, because this is the only different tungsten oxide component between the supported WZrOH and $WZrO_2$ catalyst series. Importantly, this also demonstrates that a monolayer of surface polytungstate species on ZrO_2 which is present for the model supported $WZrO_2$ catalyst series does not represent the catalytic active sites, because its TOF for the supported $WZrO_2$ series is a factor of ~10^1–10^2 lower than that of the monolayer-covered supported WZrOH catalyst, which also contains some Zr-stabilized distorted WO_3 NPs (see Fig. 13). The supported WZrOH catalyst with the highest TOF corresponds to $\rho_{W,surf}$ ~ 6 W-atoms/nm^2, just above monolayer coverage, where crystalline WO_3 NPs are expected. The corresponding Raman spectra reveals that generally, only Zr-stabilized WO_3 NPs are present for all of the supported WZrOH catalyst samples at $\rho_{W,surf} \leqslant 7$ W-atoms/nm^2. The lower TOF/TOR activity of the supported WZrOH catalysts with $\rho_{W,surf} > 9$ W-atoms/nm^2 is associated with the presence of bulk-like crystalline WO_3 particles, which have only modest acidic activity, and probably are also covering up some of the more active catalytic surface sites (see Fig. 13). The supported WZrOH catalysts are still significantly more active than the model supported $WZrO_2$ catalysts for $\rho_{W,surf} > 9$ W-atoms/nm^2 because of the presence of some distorted Zr-WO_3 NPs that are not present in the model supported $WZrO_2$ catalyst system. This also is demonstrated in further studies in which introduction of Zr-WO_3 NPs into the model $WZrO_2$ catalyst was found to increase the TOF by as much as a factor of 10^2.

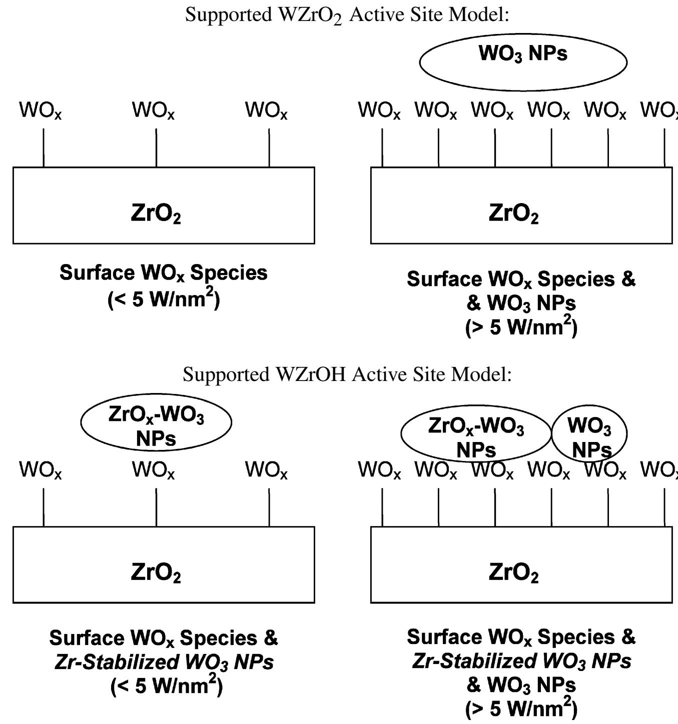

Scheme 1. Proposed catalytic active sites present in supported WO_3/ZrO_2 catalysts. Surface WO_x species represents monotungstate and polytungstate surface $O{=}W(–O–)_4$ species, with the latter predominating above low surface WO_x coverage.

Previous studies with similar supported WZrOH catalysts have proposed that the acidic catalytic activity of supported WZrOH catalysts for *o*-xylene isomerization and 2-butanol dehydration is only a function $\rho_{W,surf}$ and corresponds to a two-dimensional surface polytungstate monolayer present in a partially reduced state [18–22,25–29,31]. However, the most active and least active TOFs for supported WZrOH catalysts for methanol dehydration, have the same $\rho_{W,surf}$ values at ~6 W-atoms/nm^2 (see Fig. 13), indicating that something besides just the $\rho_{W,surf}$ parameter influences the catalytic activity. This is further supported by the orders of magnitude difference in TOF/TOR values for the supported WZrOH and model supported $WZrO_2$ catalysts at the same $\rho_{W,surf}$ value (see Fig. 13). The only significant difference between the supported WZrOH series and the model supported $WZrO_2$ series is the presence of Zr-stabilized distorted WO_3 NPs in the former, which are the catalytically active sites for the supported WZrOH catalysts. The insensitivity of the methanol dehydration TOF to the gas-phase O_2 pressure also is inconsistent with the need for weakly reduced acidic catalytic active sites; *in situ* UV–vis reveals that all of the supported WO_x species are fully oxidized in the presence of molecular O_2, and reduced sites are present in the absence of O_2. The new model proposed here with Zr-stabilized distorted WO_3 NPs as the catalytic active sites for supported WZrOH catalysts is consistent with all of the experimental observations.

5. Conclusion

The supported WZrOH catalyst system attains monolayer coverage at $\sim$5 W-atoms/nm^2. In the sub-monolayer region, dehydrated surface WO_x species and some Zr-stabilized distorted WO_3 NPs are present. The surface WO_x species rapidly become polymerized with increasing surface coverage, and surface polytungstates become the dominant species at modest surface coverage. Above the monolayer region, the supported WZrOH catalysts have the surface polytungstate monolayers, with distorted Zr-WO_3 NPs and ordered crystalline WO_3 NPs. With increasing $\rho_{W,surf}$ and calcination temperature, their relative concentrations vary accordingly: crystalline WO_3 > Zr-stabilized distorted WO_3 NPs > surface polytungstate species. Comparison of the structural characterization information with the acid-catalyzed methanol dehydration performance reveals that the distorted Zr-WO_3 NPs are responsible for the enhanced catalytic activity of supported WZrOH catalysts over the model supported ZrO_2 catalysts. The maximum concentration of the Zr-stabilized distorted WO_3 NPs corresponds to $\sim$6–7 W-atoms/nm^2, which is just above monolayer coverage.

Acknowledgments

This work was supported by the National Science Foundation's Nanoscale Interdisciplinary Research Team (NSF-NIRT) under Grant 0609018. The authors thank their colleagues at Lehigh University's *Operando* Molecular Spectroscopy and Catalysis Laboratory for their helpful discussions, particularly Professor Jih-Mirn Jehng for the amorphous WO_3 Raman studies. Two of the authors (M.S.W. and W.V.K.) acknowledge additional support from SABIC Americas.

References

[1] M. Hino, K. Arata, J. Chem. Soc. Chem. Commun. 18 (1988) 1259.
[2] J.G. Santiesteban, J.C. Vartuli, S. Han, R.D. Bastian, C.D. Chang, J. Catal. 168 (2) (1997) 431.
[3] M. Hino, K. Arata, Chem. Lett. 6 (1989) 971.
[4] R.A. Boyse, E.I. Ko, J. Catal. 171 (1997) 191.
[5] C.D. Chang, C.T. Kresge, J.G. Santiesteban, J.C. Vartuli, U.S. Patent No. 5,510,309 (1996).
[6] C.D. Chang, J.G. Santiesteban, D.L. Stern, U.S. Patent No. 5,719,097 (1998).
[7] C.D. Chang, F.T. DiGuiseppi, J.G. Santiesteban, U.S. Patent No. 5,780,382 (1998).
[8] C.D. Chang, F.T. DiGuiseppi, S. Han, J.G. Santiesteban, D.L. Stern, U.S. Patent No. 5,854,170 (1998).
[9] C.D. Chang, J.G. Santiesteban, D.L. Stern, U.S. Patent No. 6,080,904 (2000).
[10] R.D. Gillespie, U.S. Patent No. 6,818,589 B1 (2004).
[11] R.D. Gillespie, U.S. Patent No. 6,977,322 B2 (2005).
[12] C.D. Chang, J.G. Santiesteban, D.S. Shihabi, S.A. Stevenson, U.S. Patent No. 5,401,478 (1995).
[13] C.D. Chang, J.G. Santiesteban, D.S. Shihabi, D.L. Stern, J.C. Vartuli, U.S. Patent No. 5,552,128 (1996).
[14] C.D. Chang, F.T. DiGuiseppi, S. Han, U.S. Patent No. 5,563,310 (1996).
[15] C.D. Chang, S. Han, J.G. Santiesteban, M.M. Wu, Y. Xiong, U.S. Patent No. 5,453,556 (1995).
[16] C.D. Chang, S. Han, D.J. Martenak, J.G. Santiesteban, D.E. Walsh, U.S. Patent No. 5,543,036 (1996).
[17] M. Scheithauer, T.K. Cheung, R.E. Jentoft, R.K. Grasselli, B.C. Gates, H. Knozinger, J. Catal. 180 (1998) 1.
[18] D.G. Barton, S.L. Soled, G.D. Meitzner, G.A. Fuentes, E. Iglesia, J. Catal. 181 (1999) 57.
[19] D.G. Barton, S.L. Soled, E. Iglesia, Top. Catal. 6 (1998) 87.
[20] C.D. Baertsch, S.L. Soled, E. Iglesia, J. Phys. Chem. B 105 (7) (2001) 1320.
[21] C.D. Baertsch, K.T. Komala, Y.H. Chua, E. Iglesia, J. Catal. 205 (1) (2002) 44.
[22] D.G. Barton, M. Shtein, R.D. Wilson, S.L. Soled, E. Iglesia, J. Phys. Chem. B 103 (1999) 630.
[23] S. Kuba, P. Lukinskas, R.K. Grasselli, B.C. Gates, H. Knozinger, J. Catal. 216 (2003) 353.
[24] R.D. Wilson, D.G. Barton, C.D. Baertsch, E. Iglesia, J. Catal. 194 (2000) 175.
[25] M. Scheithauer, R.K. Grasselli, H. Knozinger, Langmuir 14 (11) (1998) 3019.
[26] E. Iglesia, D.G. Barton, S.L. Soled, S. Miseo, J.E. Baumgartner, W.E. Gates, G.A. Fuentes, G.D. Meitzner, in: 11th International Congress on Catalysis—40th Anniversary, 1996, Part A, Stud. Surf. Sci. Catal. 101 (1996) 533.
[27] C.D. Baertsch, R.D. Wilson, D.G. Barton, S.L. Soled, E. Iglesia, in: International Congress on Catalysis, 2000, Part D, Stud. Surf. Sci. Catal. 130 (2000) 3225.
[28] J.C. Vartuli, J.G. Santiesteban, P. Traverso, N. Cardona-Martinez, C.D. Chang, S.A. Stevenson, J. Catal. 187 (1) (1999) 131.
[29] D.C. Calabro, J.C. Vartuli, J.G. Santiesteban, Top. Catal. 18 (3–4) (2002) 231.
[30] I.E. Wachs, in: J.L.G. Fierro (Ed.), Metal Oxides: Chemistry and Applications, Taylor & Francis Group, LLC, Boca Raton, 2006, pp. 1–30.
[31] J. Macht, C.D. Baertsch, M. May-Lozano, S.L. Soled, Y. Wang, E. Iglesia, J. Catal. 227 (2004) 479.
[32] M.S. Wong, in: J.L.G. Fierro (Ed.), Metal Oxides: Chemistry and Applications, Taylor & Francis Group, LLC, Boca Raton, 2006, p. 31.
[33] C.D. Chang, J.G. Santiesteban, D.L. Stern, U.S. Patent No. 5,345,026 (1993).
[34] G.S. Wong, D.D. Kragten, J.M. Vohs, J. Phys. Chem. B 105 (7) (2001) 1366.
[35] V.M. Benitez, J.C. Yori, C.R. Vera, C.L. Pieck, J.M. Grau, J.M. Parera, Ind. Eng. Chem. Res. 44 (6) (2005) 1716.
[36] N. Vaidyanathan, M. Houalla, D. Hercules, Surf. Interface Anal. 26 (1998) 415.
[37] I.E. Wachs, T. Kim, E.I. Ross, Catal. Today 116 (2006) 162.
[38] T. Kim, A. Burrows, C.J. Kiely, I.E. Wachs, J. Catal. 246 (2007) 370.
[39] S. Brunauer, P.H. Emmett, E. Teller, J. Am. Chem. Soc. 60 (2) (1938) 309.
[40] R.C. Garvie, P.S. Nicholson, J. Am. Ceram. Soc. 55 (6) (1972) 303.

[41] H. Toraya, M. Yoshimura, S. Sōmiya, J. Am. Ceram. Soc. 67 (6) (1987) C119.
[42] P. Kubelka, F. Munk, Z. Tech. Phys. 12 (1931) 593.
[43] W.N. Delgass, G.L. Haller, R. Kellerman, J.H. Lunsford, Spectroscopy in Heterogeneous Catalysis, Academic Press, New York, 1979, p. 86.
[44] X. Gao, I.E. Wachs, J. Phys. Chem. B 104 (2000) 1261.
[45] E.I. Ross-Medgaarden, I.E. Wachs, in preparation.
[46] M. Valigi, D. Gazzoli, I. Pettiti, G. Mattei, S. Colonna, S. De Rossi, G. Ferraris, Appl. Catal. A Gen. 231 (1–2) (2002) 159.
[47] H.T. Rijnten, Phys. Chem. Aspects Adsorbents Catal. (1970) 315.
[48] K.T. Jung, A.T. Bell, J. Mol. Catal. A Chem. 163 (1–2) (2000) 27.
[49] N. Vaidyanathan, D.M. Hercules, M. Houalla, Anal. Bioanal. Chem. 373 (7) (2002) 547.
[50] A. Cimino, D. Gazzoli, M. Valigi, J. Electron Spectrosc. Relat. Phenom. 104 (1–3) (1999) 1.
[51] F. Kerkhof, J.A. Moulijn, J. Phys. Chem. 83 (12) (1979) 1612–1619.
[52] M. Occhiuzzi, D. Cordischi, D. Gazzoli, M. Valigi, P.C. Hydorn, Appl. Catal. A Gen. 269 (2004) 169.
[53] V.G. Keramidas, W.B. White, J. Am. Ceram. Soc. 57 (1) (1974) 22–24.
[54] D.P.C. Thackeray, Spectrochim. Acta Part A 30 (2) (1974) 549.
[55] E.I. Ross-Medgaarden, I.E. Wachs, J. Phys. Chem. C 111 (2007) 15089.
[56] E. Cazzanelli, C. Vinegoni, G. Mariotto, A. Kuzmin, J. Purans, J. Solid State Chem. 142 (1) (1999) 24.
[57] J.A. Horsley, I.E. Wachs, J.M. Brown, G.H. Via, F.D. Hardcastle, J. Phys. Chem. 91 (1987) 4014.
[58] J.M. Tatibouet, J. Appl. Catal. A Gen. 148 (1997) 205.
[59] D.S. Kim, M. Ostromecki, I.E. Wachs, J. Mol. Catal. A Chem. 106 (1996) 93.
[60] F. DiGregorio, V. Keller, J. Catal. 225 (2004) 45.
[61] V. Lebarbier, G. Clet, M. Houalla, J. Phys. Chem. B 110 (2006) 13905.
[62] I.E. Wachs, Catal. Today 27 (1996) 437.
[63] L. Salvati, L.E. Makovsky, J.M. Stencel, F.R. Brown, D.M. Hercules, J. Phys. Chem. 85 (1981) 3700.
[64] M.M. Ostromecki, L.J. Burcham, I.E. Wachs, J. Mol. Catal. A Chem. 132 (1998) 59.
[65] Y.S. Chen, I.E. Wachs, J. Catal. 217 (2003) 468.
[66] N. Vaidyanathan, M. Houalla, D.M. Hercules, Catal. Lett. 43 (1997) 209.
[67] C. Pfaff, M.J. Perez-Zurita, C. Scott, P. Patino, M.R. Goldwasser, J. Goldwasser, F.M. Mulcahy, M. Houalla, D.M. Hercules, Catal. Lett. 49 (1997) 13.
[68] N. Naito, N. Katada, M. Niwa, J. Phys. Chem. B 103 (1999) 7206.
[69] X.F. Yu, N.Z. Wu, H.Z. Huang, Y.C. Xie, Y.Q. Tang, J. Mater. Chem. 11 (2001) 3337.
[70] J. Engweiler, J. Harf, A. Baiker, J. Catal. 159 (1996) 256.
[71] G. Bond, S. Flamerz, L. van Wijk, Catal. Today 1 (1987) 229.
[72] S.S. Chan, I.E. Wachs, L.L. Murrell, N.C. Dispenziere Jr., J. Catal. 92 (1985) 1.
[73] J. Dobler, M. Pritzsche, J. Sauer, J. Am. Chem. Soc. 127 (2005) 10861.